

## exoALMA XX: Tomographic Detection of Embedded Planets in Protoplanetary Disks

ANDRÉS F. IZQUIERDO <sup>1,2,\*</sup> JAEHAN BAE <sup>1</sup> STEFANO FACCHINI <sup>3</sup> EWINE F. VAN DISHOCK <sup>2,4</sup>  
MARCELO BARRAZA-ALFARO <sup>5</sup> MYRIAM BENISTY <sup>6</sup> RICHARD TEAGUE <sup>5</sup> JOCHEN STADLER <sup>7,8</sup>  
SEAN M. ANDREWS <sup>9</sup> GIANNI CATALDI <sup>10</sup> NICOLÁS CUELLO <sup>11</sup> PIETRO CURONE <sup>12</sup> IAN CZEKALA <sup>13</sup>  
DANIELE FASANO <sup>7</sup> MARIO FLOCK <sup>6</sup> MISATO FUKAGAWA <sup>14</sup> MARIA GALLOWAY-SPRIETSMAN <sup>1</sup>  
CASSANDRA HALL <sup>15,16,17</sup> JANE HUANG <sup>18</sup> JOHN D. ILEE <sup>19</sup> ANDREA ISELLA <sup>20,21</sup> JENSEN LAWRENCE <sup>5</sup>  
GEOFFROY LESUR <sup>11</sup> GIUSEPPE LODATO <sup>3</sup> CRISTIANO LONGARINI <sup>22</sup> RYAN A. LOOMIS <sup>23</sup> FRANÇOIS MÉNARD <sup>11</sup>  
CHRISTOPHE PINTÉ <sup>11,24</sup> DANIEL J. PRICE <sup>24</sup> GIOVANNI ROSOTTI <sup>3</sup> LEONARDO TESTI <sup>25</sup> DAVID J. WILNER <sup>9</sup>  
ANDREW J. WINTER <sup>26</sup> LISA WÖLFER <sup>5</sup> AND BRIANNA ZAWADZKI <sup>27</sup>

<sup>1</sup>Department of Astronomy, University of Florida, Gainesville, FL 32611, USA; [andres.izquierdo.c@gmail.com](mailto:andres.izquierdo.c@gmail.com)

<sup>2</sup>Leiden Observatory, Leiden University, P.O. Box 9513, NL-2300 RA Leiden, The Netherlands

<sup>3</sup>Dipartimento di Fisica, Università degli Studi di Milano, Via Celoria 16, 20133 Milano, Italy

<sup>4</sup>Max-Planck Institut für Extraterrestrische Physik (MPE), Gießenbachstr. 1, 85748 Garching bei München, Germany

<sup>5</sup>Department of Earth, Atmospheric, and Planetary Sciences, Massachusetts Institute of Technology, Cambridge, MA 02139, USA

<sup>6</sup>Max-Planck Institute for Astronomy (MPIA), Königstuhl 17, 69117 Heidelberg, Germany

<sup>7</sup>Université Côte d'Azur, Observatoire de la Côte d'Azur, CNRS, Laboratoire Lagrange, 06304 Nice, France

<sup>8</sup>European Southern Observatory, Karl-Schwarzschild-Str. 2, D-85748 Garching bei München, Germany

<sup>9</sup>Center for Astrophysics — Harvard & Smithsonian, Cambridge, MA 02138, USA

<sup>10</sup>National Astronomical Observatory of Japan, 2-21-1 Osawa, Mitaka, Tokyo 181-8588, Japan

<sup>11</sup>Univ. Grenoble Alpes, CNRS, IPAG, 38000 Grenoble, France

<sup>12</sup>Departamento de Astronomía, Universidad de Chile, Camino El Observatorio 1515, Las Condes, Santiago, Chile

<sup>13</sup>School of Physics & Astronomy, University of St. Andrews, North Haugh, St. Andrews KY16 9SS, UK

<sup>14</sup>National Astronomical Observatory of Japan, Osawa 2-21-1, Mitaka, Tokyo 181-8588, Japan

<sup>15</sup>Department of Physics and Astronomy, The University of Georgia, Athens, GA 30602, USA

<sup>16</sup>Center for Simulational Physics, The University of Georgia, Athens, GA 30602, USA

<sup>17</sup>Institute for Artificial Intelligence, The University of Georgia, Athens, GA, 30602, USA

<sup>18</sup>Department of Astronomy, Columbia University, 538 W. 120th Street, Pupin Hall, New York, NY, USA

<sup>19</sup>School of Physics and Astronomy, University of Leeds, Leeds, UK, LS2 9JT

<sup>20</sup>Department of Physics and Astronomy, Rice University, 6100 Main St, Houston, TX 77005, USA

<sup>21</sup>Rice Space Institute, Rice University, 6100 Main St, Houston, TX 77005, USA

<sup>22</sup>Institute of Astronomy, University of Cambridge, Madingley Road, CB3 0HA, Cambridge, UK

<sup>23</sup>National Radio Astronomy Observatory, 520 Edgemont Rd., Charlottesville, VA 22903, USA

<sup>24</sup>School of Physics and Astronomy, Monash University, Clayton VIC 3800, Australia

<sup>25</sup>Dipartimento di Fisica e Astronomia, Università di Bologna, I-40129 Bologna, Italy

<sup>26</sup>Astronomy Unit, School of Physics and Astronomy, Queen Mary University of London, London E1 4NS, UK

<sup>27</sup>Department of Astronomy, Van Vleck Observatory, Wesleyan University, 96 Foss Hill Dr., Middletown, CT, 06459, USA

### ABSTRACT

The exoALMA Large Program has revealed a wealth of substructures in the dust and molecular line emission of several protoplanetary discs, suggesting that planet formation may unfold within highly dynamic environments. Using synthetic observations of planet-disc interactions and disc instabilities, we demonstrate how the origin of these substructures can be investigated through a tomographic study of molecular lines, extending the scope of the analysis beyond line-centroid kinematics alone. Our results indicate that with only a few hours of ALMA integration at moderate angular resolution ( $0''.15$ – $0''.30$ ), it is possible to identify the key signatures driven by planets more massive than 0.1% of the stellar mass. These signatures manifest not only as deviations from Keplerian motion but also as localized line broadening, enabling accurate constraints on the orbital radius and azimuthal location of the planets. We further show that a diagnostic based on line skewness in spectrally resolved observations can help distinguish between planetary and instability-driven signatures, owing to the distinct degrees of velocity coherence associated with each mechanism. Finally, we apply this tomographic analysis

to exoALMA CO line data for the discs of HD 135344B and MWC 758. In HD 135344B, we identify strongly localized velocity and line-width perturbations, suggesting the possibility of three massive planets embedded in the disc: one at  $R = 95$  au, exterior to the continuum substructures, and two within dust gaps at  $R = 41$  au and  $R = 73$  au. For MWC 758, the dominance of vertical-velocity spirals over localized signatures is consistent with predictions from models of moderate disc eccentricities or warps, potentially induced by a substellar companion in the inner regions of the system.

*Keywords:* Protoplanetary disks (1300); Planet formation (1241); Planetary-disk interactions (2204), Exoplanet detection methods (489)

## 1. INTRODUCTION

Sensitive and high-angular resolution ALMA observations of protoplanetary discs are revolutionizing our understanding of the physicochemical mechanisms of planet formation. These data have revealed different families of dust and gas substructures in numerous discs (Andrews et al. 2018; Öberg et al. 2021; Teague et al. 2025; Fukagawa et al. 2026), potentially arising from the interplay between thermochemical processes (e.g. Miotello et al. 2023; Öberg et al. 2023) and physical mechanisms, including planet– and star-disc interactions (see Pinte et al. 2023, for a review), as well as gravitational and (magneto)hydrodynamical disc instabilities (e.g. Lesur et al. 2023; Bae et al. 2023).

In particular, the dynamical interaction between discs and planets is known to induce distinct signatures in molecular-line data, which can be broadly categorized into two groups according to their observed symmetry. The first group comprises axisymmetric substructures dominated by azimuthal velocity flows associated with pressure modulations around planet-carved gaps (e.g. Teague et al. 2018; Rosotti et al. 2020; Izquierdo et al. 2023; Stadler et al. 2025). The second group includes non-axisymmetric patterns extending across the disc, typically in the form of spirals (e.g. Teague et al. 2021; Calcino et al. 2022; Wölfer et al. 2023), as well as localized kinematic perturbations (e.g. Pinte et al. 2018; Casassus & Pérez 2019; Izquierdo et al. 2022; Stadler et al. 2023) and chemical anomalies detected in the vicinity of embedded planets (Law et al. 2023; Izquierdo et al. 2026). A comparatively less explored feature in this group involves localized meridional flows induced by a planet, which lead to enhanced velocity dispersion. These flows arise from the interplay between planet-induced gravitational torques and viscous torques that act to refill the planet-driven gap from disc layers above the midplane (Dong et al. 2019; Izquierdo et al. 2023).

Similar observational features may, however, also arise from fluid instabilities that develop under specific disc conditions. For instance, nearly axisymmetric flows are a common outcome of the vertical shear instability (VSI; e.g. Barraza-Alfaro et al. 2021), which operates in thermally stratified discs with short cooling times that sustain differential rotation above the midplane. Spiral-like structures, by contrast, are more characteristic of gravitational instability (GI; e.g. Hall et al. 2020; Speedie et al. 2024), which occurs in sufficiently massive discs where self-gravity overcomes thermal and rotational support. Large-scale spiral morphologies, together with localized eddies, can also arise from the magnetorotational instability (MRI; e.g. Barraza-Alfaro et al. 2025), which develops in regions where the gas is sufficiently ionized for magnetic fields to couple to the flow and drive turbulence.

In this work, we quantify the detectability of planet-driven perturbations using exoALMA-like observations of three-dimensional planet-disc interaction simulations. We adopt a tomographic approach in which line broadening and line asymmetries are used as diagnostics of coherent velocity flows in the vicinity of embedded planets, and compare these signatures with those produced in VSI, MRI, and GI simulations. We then apply this analysis to two distinct exoALMA targets: the disc of HD 135344B, where multiple localized perturbations are identified, and MWC 758, where large-scale substructures predominate.

This Letter is organized as follows. Section 2 describes the observational data and channel-map models of the exoALMA targets analyzed in this study. Section 3 presents the extraction and characterization of observable features from models of planet-disc interactions and fluid instabilities. Section 4 illustrates the application of this methodology to the discs of HD 135344B and MWC 758. Section 5 discusses the interpretation of the detected signatures, and Section 6 highlights the main results of the work.

\* NASA Hubble Fellowship Program Sagan Fellow

## 2. DATA AND MODELS

The ALMA data used in this Letter consist of exoALMA continuum-subtracted Fiducial Images of  $^{12}\text{CO}$  and  $^{13}\text{CO } J = 3 \rightarrow 2$  for the discs of HD 135344B and MWC 758, as defined in Teague et al. (2025). These data cubes have a circular synthesized beam of  $0''.15$  and a channel spacing of  $0.1 \text{ km s}^{-1}$ . Details of the calibration and imaging procedures are provided in Loomis et al. (2025). We also use exoALMA Fiducial Continuum Images centered at  $0.9 \text{ mm}$  from Curone et al. (2025), and VLT/SPHERE scattered-light images presented in Stolker et al. (2016) and Benisty et al. (2015). Channel-map models of the targets produced with DISCMINER, as reported by Izquierdo et al. (2025), are used as references to compute residual maps. These residuals enable the analysis of gas substructures that manifest as non-Keplerian motions and, more generally, as perturbations in the shape of the molecular line profiles. The Keplerian stellar masses obtained from the channel-map models are  $1.61$  and  $1.40 M_{\odot}$  for HD 135344B and MWC 758, respectively, assuming Gaia-derived distances of  $135$  and  $156 \text{ pc}$  (Gaia Collaboration et al. 2023). The low disc inclinations of  $-16^{\circ}$  and  $19^{\circ}$ , as inferred with DISCMINER, render the backside emission contribution negligible for both targets, resulting in line profiles that are generally symmetric about their centroids. We therefore characterize the line peaks, centroid velocities, and line widths of both the observed and modeled spectra by fitting single-Gaussian profiles along the spectral axis at each image pixel.

## 3. ANALYSIS OF SYNTHETIC OBSERVATIONS

In this section, we present our analysis methodology for identifying gas substructures in molecular line images produced by planet-disc interactions and fluid instabilities including VSI, MRI, and GI. The simulations are postprocessed to match the observational constraints of exoALMA, allowing us to assess the detectability of the associated signatures under realistic conditions. Residual maps of the analyzed mechanisms, obtained after subtracting smooth Keplerian DISCMINER models, are shown in Figure 1, with selected  $^{12}\text{CO}$  intensity channels presented in Figure 18 of the Appendix.

### 3.1. Simulation setup and radiative transfer

The planet-disc interaction simulations explored in this work were performed using the FARGO3D code (Benítez-Llambay & Masset 2016). This choice is not critical, however, as other hydrodynamic packages produce consistent observable kinematic signatures when analyzed through the same pipeline applied here (Bae et al. 2025). The simulations are set up following Teague

et al. (2019), which aimed to reproduce the gas kinematics in the disc of HD 163296. In brief, the disc is initialized with a density distribution that satisfies the hydrostatic equilibrium and adopts a uniform alpha viscosity of  $10^{-3}$ . The disc midplane and atmosphere follow independent power-law temperature distributions with radius, connected in the vertical direction by a squared-cosine function (Dartois et al. 2003). Instead of inserting multiple planets as in Teague et al. (2019), we run two single-planet simulations with planet masses of  $M_p = 2 M_{\text{Jup}}$  and  $4 M_{\text{Jup}}$  orbiting a  $2 M_{\odot}$  star, corresponding to planet-to-star mass ratios of  $q \sim 1 \times 10^{-3}$  and  $\sim 2 \times 10^{-3}$ , respectively. The orbital radius of the planet is fixed at  $R_p = 240 \text{ au}$ , while the azimuth  $\phi_p$  is varied in eight increments of  $45^{\circ}$  to study the effects of projection and radiation transport on the retrieved perturbations along the entire disc circumference.

Radiative transfer calculations of CO line intensities were performed with RADMC3D (Dullemond et al. 2012), assuming a distance to the source of  $101 \text{ pc}$  and three disc inclinations:  $i = -15^{\circ}$ ,  $-30^{\circ}$ , and  $-45^{\circ}$ . The central star is assumed to have mass and luminosity of  $2 M_{\odot}$  and  $17 L_{\odot}$ , respectively, similar to those of HD 163296 (Fairlamb et al. 2015). We assume that CO is fully photodissociated in surface layers of the disc where the vertically integrated gas density falls below  $10^{21} \text{ cm}^{-2}$  (Visser et al. 2009), and that CO is frozen onto dust grains in regions where the temperature drops below  $21 \text{ K}$  (Schwarz et al. 2016). For the remainder of the gas disc we adopt a CO/H<sub>2</sub> abundance ratio of  $10^{-5}$ .

Synthetic observations replicating the main properties of the Fiducial Images from exoALMA were generated using the SYNDISK code<sup>1</sup>, adopting a channel spacing of  $0.1 \text{ km s}^{-1}$ , and circular beams of  $0''.15$  and  $0''.3$ . Two rms noise levels of  $1.2$  and  $2.4 \text{ K}$  were adopted for the fiducial  $0''.15$  beam, corresponding to signal-to-noise ratios (SNR) of  $\sim 15$  and  $\sim 30$  relative to the azimuthally averaged peak intensity of  $35 \text{ K}$  measured at the planet's orbital radius in the  $q \sim 2 \times 10^{-3}$ ,  $i = 15^{\circ}$  simulation. Under the same observational constraints, the larger  $0''.3$  beam also used here yields an  $8\times$  increase in SNR.

The simulations and synthetic observations of the disc instabilities studied in this work are described in detail by Barraza-Alfaro et al. (2025). They were performed using the magnetohydrodynamics code PLUTO (Mignone et al. 2007) and were originally presented by Flock et al. (2020) for the vertical shear instability (VSI), Flock et al. (2015) for the magnetorotational instability (MRI), and Béthune & Latter (2022) for gravi-

<sup>1</sup> <https://github.com/richteague/syndisk>

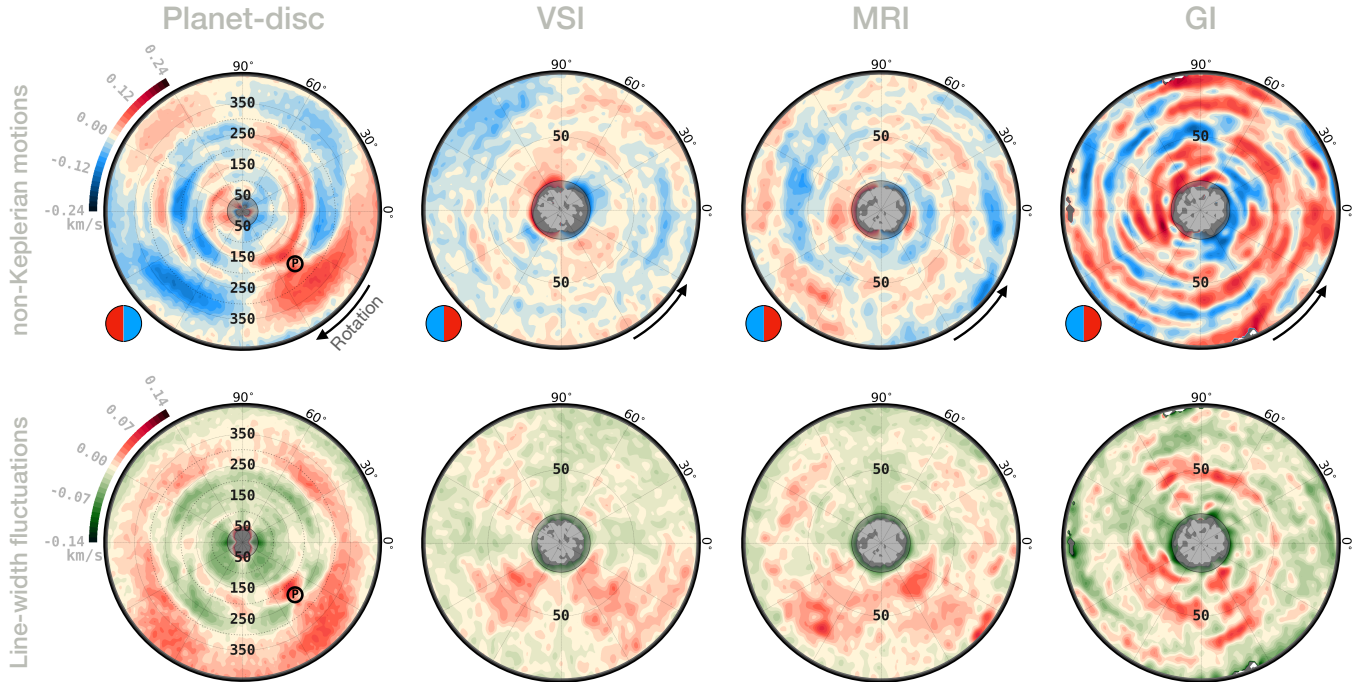


**Figure 1.** Velocity and line-width residuals derived from DISCMNER models applied to synthetic observations of planet-disc interaction ( $q = 2 \times 10^{-3}$ ,  $\phi_p = -45^\circ$ ) and disc instabilities. Details of the simulation setups are provided in Sect. 3.1. All discs are inclined by  $-30^\circ$ , and the residuals from all mechanisms are shown on the same color scale indicated on the left. Semi red-blue circles in the bottom left corners of the top-row panels indicate the locations of the redshifted and blueshifted sides of the simulated disc, which are useful to understand the velocity structure of the non-Keplerian flows (see Fig. 2).

tational instability (GI). In all cases, the adopted stellar mass was  $M_\star = 0.5 M_\odot$ , with a self-gravitating disc mass of  $0.1 M_\odot$  in the GI simulation, and a disc inclination of  $i = -30^\circ$ . For the postprocessing stage, we generate synthetic  $^{12}\text{CO } J = 3 \rightarrow 2$  emission for each mechanism using RADMC3D, assuming a source distance of 140 pc, a channel spacing of  $0.1 \text{ km s}^{-1}$ , and a  $^{12}\text{CO}$  abundance of  $10^{-4}$ , reduced by a factor of  $10^5$  in regions of the disc where the temperature falls below 21 K (to emulate CO freeze-out) or where the vertically integrated gas column density drops below  $10^{21} \text{ cm}^{-2}$  (to account for CO photodissociation). Since the physical domains of the simulations are typically smaller ( $\sim 100 \text{ au}$ ) than those of most exoALMA discs, the angular resolution of the synthetic observations was set to  $0''.035$  in order to sample the disc radial extent with  $\sim 20$  resolution elements, consistent with the average of our targets. The rms noise level was set to 1.3 K, yielding signal-to-noise ratios between 15 and 30 relative to the measured peak intensities across the disc.

### 3.2. *Folded maps and Localized signatures*

Embedded planets are known to induce localized perturbations in the dynamical and physical structure of their host discs (e.g. Pérez et al. 2018; Dong et al. 2019).

To identify such signatures in our simulated data, we search for high-amplitude, spatially clustered residuals in folded velocity and line-width maps following the approach of Izquierdo et al. (2021). By applying this folding procedure, which compares two-dimensional maps of these line-profile properties on the redshifted and blueshifted sides of the disc, we can selectively isolate non-axisymmetric perturbations driven by planets and other mechanisms.

*Folded maps*—For velocities, folded maps can be constructed either by adding or subtracting one side of the disc from the other, depending on which velocity components are to be suppressed. As illustrated in Figure 2, additive folding minimizes the contribution of axisymmetric azimuthal velocity flows (e.g. those prominent around gas gaps, Izquierdo et al. 2023; Benisty et al. 2026), whereas subtractive folding is more effective at filtering out axisymmetric vertical or radial velocity components (e.g. Stadler et al. 2023). Since azimuthal velocity flows typically dominate around surface density gaps (Stadler et al. 2025) and on global scales primarily due to the disc Keplerian rotation (Longarini et al. 2025), we adopt additive folding as the default method for reducing velocity maps unless otherwise specified. Conversely, because line width is a scalar quantity, we search for lo-

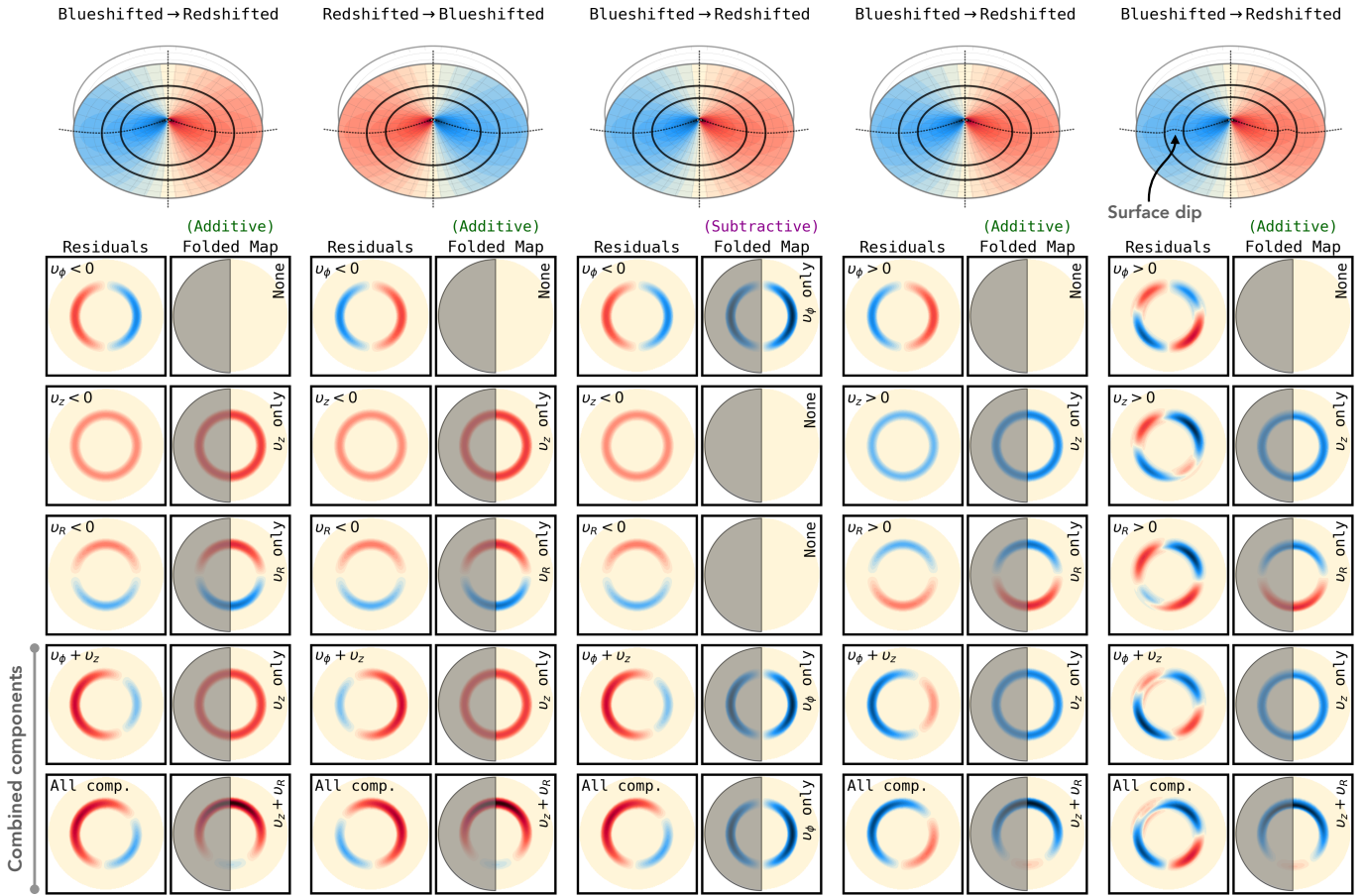


**Figure 2.** Illustrating axisymmetric velocity residuals for different combinations of velocity components, projected disc rotation, and the resulting folded maps obtained using either the additive or subtractive folding method. The first three columns show residuals for negative velocity flows after subtraction of a Keplerian model, while the following two focus on positive ones. In this context, *positive* denotes super-Keplerian motion for  $v_\phi$ , outward motion in cylindrical radius for  $v_R$ , and upward motion relative to the disc midplane for  $v_z$ . The rightmost column shows a scenario where the underlying disc emission surface includes a dip (30 au wide and 20 au deep) that is not considered by the subtracted model. This substructure introduces an anti-symmetric contribution to the residuals around the disc minor axis, which is consequently filtered out after additive folding.

calized enhancements in this property using subtractive folding. Peak intensities are excluded from this analysis, as for the optically thick line adopted they respond more strongly to large-scale temperature fluctuations than to the local influence of the planet. However, they may still be valuable for optically thinner tracers that probe closer to the midplane, where they can capture both temperature and density anomalies in the planet’s vicinity.

*Localized signatures*—We take the locations of global peak residuals as proxies for embedded planets. These are derived from a two-dimensional distribution of peak velocity and line-width values extracted per annulus from the folded maps, with annuli spaced at intervals of one-fifth of the beam size. A global peak is considered significant when it exceeds  $3\sigma$  relative to the mean value of all identified peaks, where  $\sigma$  denotes the standard deviation of the peak distribution. As a less conservative

alternative, and to avoid bias from the candidate itself inflating the noise value, we additionally evaluate a scatter estimator of the peak distribution ( $p$ ) based on the median absolute deviation (MAD), defined as

$$\sigma_{\text{MAD}} = 1.4826 \times \text{median}(|p - \text{median}(p)|) \quad (1)$$

which provides a Gaussian-equivalent estimate of the standard deviation for normally distributed data while remaining insensitive to a small number of outliers (e.g. [Leys et al. 2013](#)), such as planet-induced peaks. Hence,  $\sigma_{\text{MAD}}$  offers a more representative measure of the background disc perturbations away from the planet vicinity.

We also apply a K-means algorithm to identify localized clusters of residuals across both the azimuthal and radial extents of the disc as additional indicators of planet locations. The clustering analysis uses the same distribution of peak velocity and line-width residuals extracted from the folded maps. A cluster is classified as

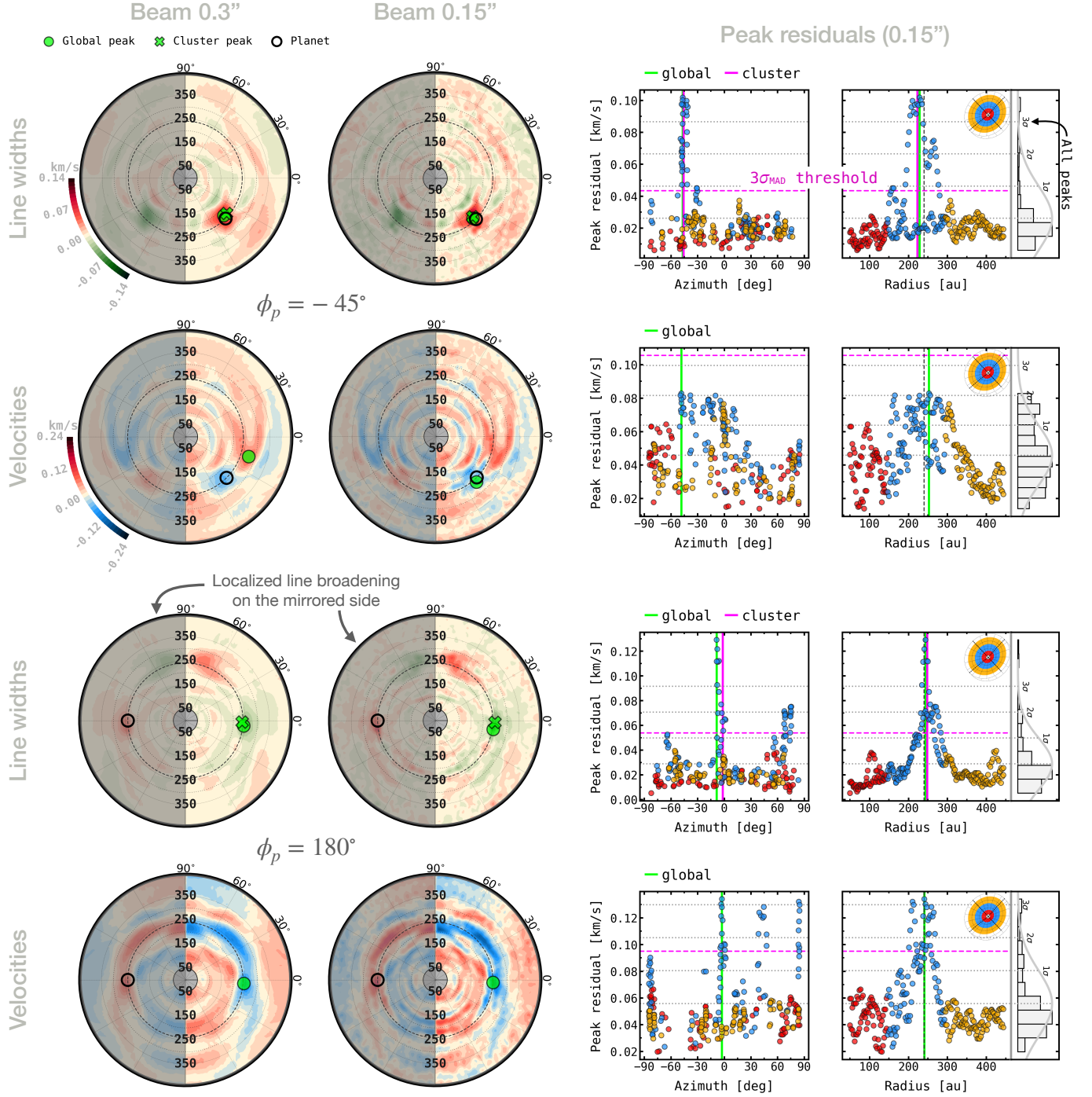


**Figure 3.** Illustration of the localized signatures identified in folded line-width and velocity residuals traced by  $^{12}\text{CO}$  emission from a planet-disc interaction simulation with a planet-to-star mass ratio of  $q \sim 2 \times 10^{-3}$ , assuming a disc inclination of  $i = -30^\circ$ . Results are shown for two planet azimuths,  $\phi_p = -45^\circ$  and  $180^\circ$ , and for two beam sizes,  $0.3''$  and  $0.15''$ . Green circles and crosses mark the locations of peak and clustered residuals, while the unfilled circle denotes the true planet position. A signal is considered detected when its global peak exceeds a significance of  $3\sigma$ , as indicated by the horizontal dotted and dashed lines, corresponding to thresholds defined using all peak residuals and the MAD estimator, respectively. Detections based on line widths have a higher success rate due to their stronger spatial localization (clustered residuals), compared to their velocity counterparts, which in this example remain undetected for the  $\phi_p = -45^\circ$  planet and only marginally detected for  $\phi_p = 180^\circ$ . Since embedded planets are expected to produce localized line-width enhancements rather than reductions, the sign of the line-width signal also helps resolve the ambiguity between opposite sides of the disc introduced by the folding process.

significantly localized and coherent when its variance exceeds the mean variance of all other clusters identified in the disc by more than  $3\sigma$ , where  $\sigma$  denotes the standard deviation of the cluster-to-cluster variance distribution.

### 3.2.1. Planet-driven signatures

Figure 3 illustrates a subset of the folded maps obtained from our planet-disc interaction models, highlighting the localized line-width and velocity signatures induced by the embedded planet. These maps correspond to models with a planet-to-star mass ratio of  $q \sim 2 \times 10^{-3}$  and are extracted from images convolved to beam sizes of  $0''.15$  (with  $\text{SNR} \sim 30$ ) and  $0''.3$ , assuming a disc inclination of  $i = -30^\circ$ .

*Line width vs. velocity signals*—For the  $0''.15$  beam, detections based on line-width residuals are successful for all eight planet azimuths considered, with median offsets of 6.2 au in radius (i.e. less than half a beam width) and  $6.0^\circ$  in azimuth relative to the true planet position. The corresponding median detection significances across planet azimuths are  $4.3\sigma$  with respect to all peak residuals and  $8.3\sigma$  when referenced to the scatter estimate  $\sigma_{\text{MAD}}$  (Eq. 1), which is less sensitive to the strong outliers associated with the planet signal. Under the same setup, these metrics are considerably improved for an inclination of  $i = -15^\circ$ , yielding median offsets of 0.9 au in radius and  $1.5^\circ$  in azimuth, and median detection significances of  $5.3\sigma$  relative to all peaks and  $15.5\sigma$  with the MAD estimator. For  $i = -30^\circ$ , the line-width signals are detected as highly clustered in six of the eight planet azimuths; planets at  $\phi_p = -135^\circ$  and  $\phi_p = -90^\circ$  are identified only through global peak values. For  $i = -15^\circ$ , planets at all azimuths are detected using both global peak and clustered residuals.

Detections based on velocity residuals are significantly less robust, with success rates of 2/8 and 4/8 for inclinations of  $i = -30^\circ$  and  $i = -15^\circ$ , respectively. They also yield considerably lower significances than those based on line widths. For the detected signals at  $i = -30^\circ$ , we obtain a median significance of  $3.1\sigma$  relative to all peaks and  $6.1\sigma$  using the MAD estimator, while at  $i = -15^\circ$  the corresponding values are  $3.1\sigma$  and  $4.3\sigma$ . The similarity between the all-peak and MAD significances indicates that the peak velocity residuals are more nearly normally distributed than the line-width residuals, implying a weaker dominance of the planet-driven signal with respect to background disc fluctuations.

This behavior arises because strong velocity perturbations develop not only in the immediate vicinity of the planet but also at larger radial and azimuthal separations, particularly for high-mass planets or in the presence of fluid instabilities. A similar result was re-

ported by Izquierdo et al. (2021), who showed that the signals induced by their most massive planet ( $3M_{\text{Jup}}$ , or  $q \sim 3 \times 10^{-3}$ ) were less localized in velocity than those produced by lower-mass planets. Crucially, we note that this effect is likely further exacerbated by the large-scale vertical motions driven by the planet, which were not included in the two-dimensional simulations of Izquierdo et al. (2021). Additionally, as illustrated in Figure 19 in the Appendix, this effect can be amplified by projection: depending on the planet’s azimuthal location, multiple velocity components may add coherently (or destructively) along the line of sight at regions far from (or near) the planet, thereby competing with the localized signal associated with the embedded object.

Despite these challenges, velocity residuals remain a valuable diagnostic of planet presence. As shown in Figure 20 of the Appendix, although the velocity perturbations around the modeled planet are not strongly localized relative to background fluctuations, they still respond to the large-scale pressure modulation associated with the carved gap, and produce pronounced azimuthal gradients linked to the planet-induced Doppler flip, defined as a local reversal in the sign of the velocity signal across the planet location (e.g. Pérez et al. 2018; Rabago & Zhu 2021; Izquierdo et al. 2022).

*Line-width signal vs. planet azimuth and beam size*—By contrast with velocity residuals, the amplitude of the detected line-width signals shows a minimal dependence on the planet’s azimuth, as demonstrated in Figure 4, making it a more direct proxy for planet mass. An additional advantage of this diagnostic is its robustness to beam size; although degrading the angular resolution reduces the observed amplitude of the perturbations, their detectability remains largely unaffected. For a planet-to-star mass ratio of  $q \sim 2 \times 10^{-3}$ , we estimate a decrease in the median peak line width across planet azimuths from  $124 \text{ m s}^{-1}$  at a beam size of  $0''.15$  to  $74 \text{ m s}^{-1}$  at  $0''.3$ . However, in all cases, the coarser beam does not compromise the accuracy of the recovered planet location, highlighting the feasibility of systematically searching for planets even in lower-resolution data or in images deliberately degraded to improve the SNR.

*Planet mass detection limit*—The line-width peaks from the  $q \sim 1 \times 10^{-3}$  hydro models are typically identified near the true planet azimuths but lie close to the  $3\sigma$  threshold relative to both the all-peak and background (MAD) fluctuations. This suggests that a planet with a mass comparable to Jupiter orbiting a Solar-mass star provides a reasonable lower bound for the detection of planet-driven line broadening at the adopted orbital radius and under the observational constraints of

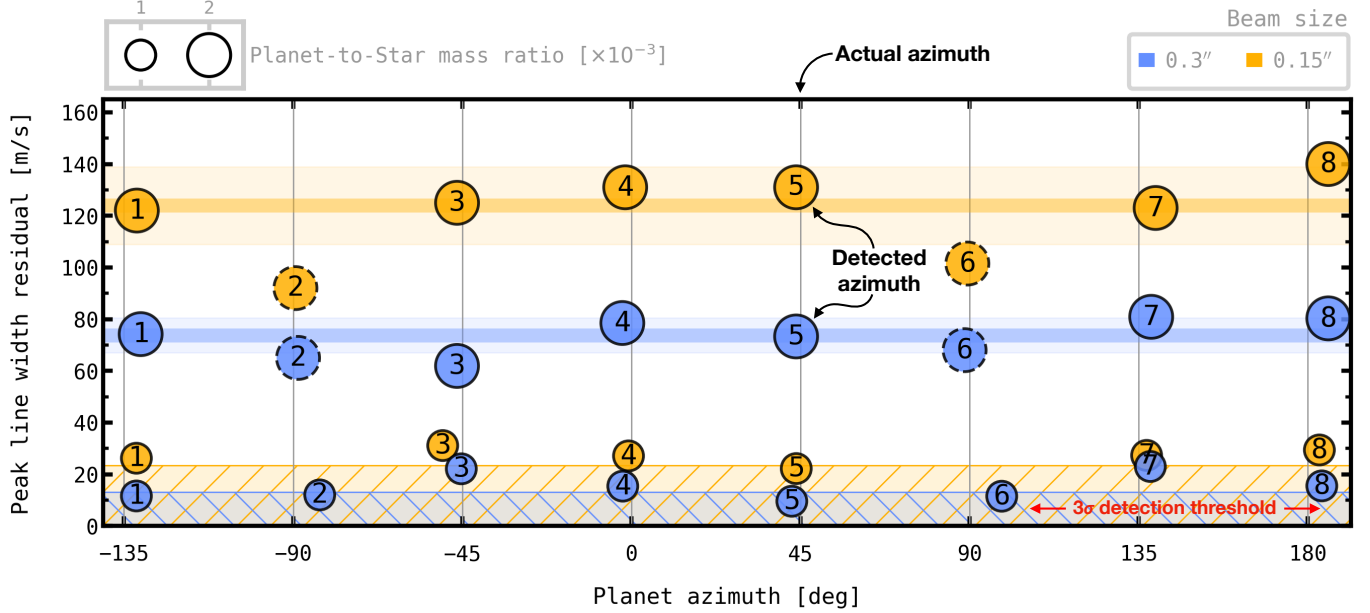


**Figure 4.** Detected amplitude of folded line-width perturbations as a function of the inferred planet azimuth in synthetic observations of the planet-disc interaction simulations introduced in Sect. 3.1, for different planet masses and beam sizes, and a disc inclination of  $i = -15^\circ$ . Although increasing the beam size from  $0''.15$  to  $0''.3$  weakens the observed signal around the planet, its detectability is not compromised, suggesting that relatively inexpensive ALMA observations are sufficient to robustly detect planets with 0.2% the mass of the star and marginally detect those with 0.1%. Line-width amplitudes shown as filled circles were measured using subtractive folding of the disc, whereas dotted circles, corresponding to planets located along the disc minor axis, were obtained using additive folding (followed by division by two) to avoid self-subtraction of the signal in the former method. Vertical lines indicate the true planet azimuths used in each of the eight simulation snapshots. Horizontal lines and shaded regions denote the median and standard deviation of the peak values, respectively, while hatched areas mark the median  $3\sigma$  detection threshold for the low-mass planet simulations.

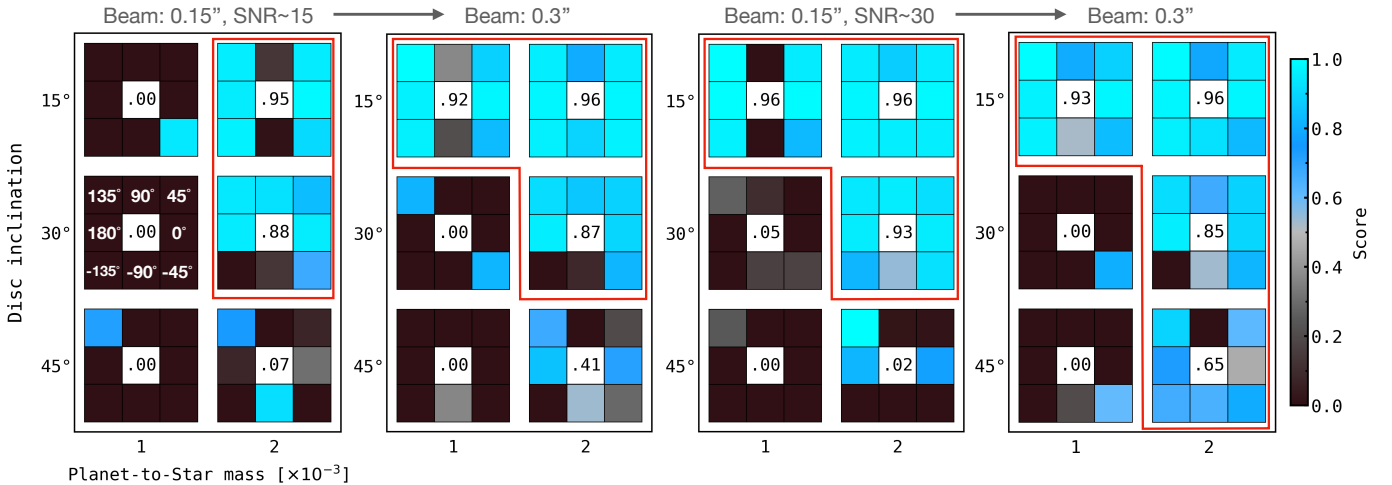


**Figure 5.** Goodness of planet detections based on localized line widths across all disc inclinations, planet masses and azimuths, beam sizes, and signal-to-noise ratios (SNR) considered. Sub-squares represent the eight adopted planet azimuths (from  $-135^\circ$  to  $180^\circ$  in steps of  $45^\circ$ ). A score of 1 corresponds to a planet detected at its true location with a significance of at least  $3\sigma$ . The score is defined as the product of three Gaussian functions evaluating the proximity of the detection in radial and azimuthal coordinates, as well as its significance. Planets with scores above 0.6 (blue sub-squares) are detected within their radial pressure bump and azimuthal sector, with a significance of at least  $3\sigma$ . Central sub-squares indicate the median score across all planet azimuths, with those exceeding 0.6 outlined in red to highlight the inclination-mass configurations where planet-driven line broadening is detectable for each adopted beam size and SNR.

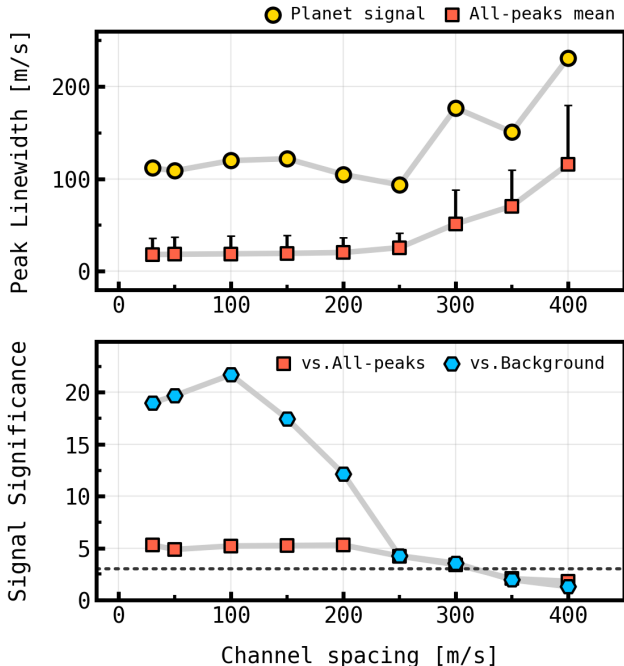


**Figure 6.** Peak line-width residual as a function of channel spacing for the planet-disc interaction model with a planet-to-star mass ratio of  $q = 2 \times 10^{-3}$ , an inclination of  $i = -15^\circ$ , and a planet azimuth of  $\phi_p = -45^\circ$ , imaged with a beam size of  $0''.15$  and an SNR of  $\sim 30$  (at  $\Delta v = 0.1 \text{ km s}^{-1}$ ). Also shown is the detection significance of the signal relative to the full distribution of peak residuals and to the median absolute deviation (MAD) of the background, which is considerably less affected by planet-driven outliers.

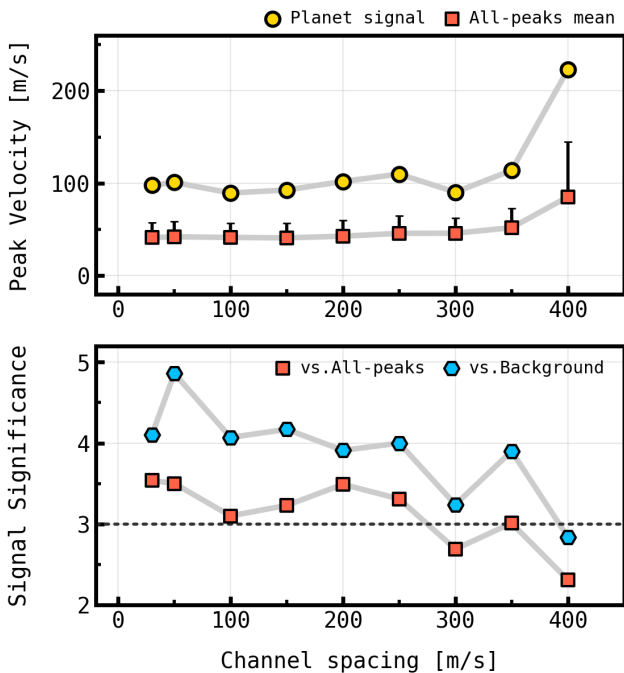


**Figure 7.** As Fig. 6 but for peak velocity residuals.

exoALMA. This estimate is consistent with the lowest-mass planet independently inferred by Pinte et al. (2025) to reproduce kink-like features in channel maps of the exoALMA targets.

*Detection robustness across parameter space*—We extend this analysis by summarizing the robustness of line-width peak detections across all adopted disc inclinations, signal-to-noise ratios, planet masses, azimuths, and beam resolutions in Figure 5. This is quantified using a scoring system ranging from 0 to 1, where a score of 1 corresponds to a detection located exactly at the planet’s true position with a significance of at least  $3\sigma$ . The score is defined as the product of three unit-amplitude Gaussian functions that evaluate the detection’s proximity to the planet in radial and azimuthal coordinates, as well as its significance. The two spatial Gaussians adopt standard deviations of  $\sigma_r = 35 \text{ au}$ , corresponding to half the radial width of the pressure modulation induced by the planet (or 1–2 beams), and  $\sigma_\phi = 20^\circ$ , equivalent to an azimuthal slice of 1/18th of the disc circumference. The significance Gaussian is capped at  $3\sigma$  and decreases normally for lower values, making the metric only weakly dependent on the choice of scatter estimator ( $\sigma$  or  $\sigma_{\text{MAD}}$ ) introduced in Sect. 3.2. Under these definitions, any planet with a score above 0.6 (blue squares) satisfies the condition of being detected within its radial pressure bump and azimuthal sector, with a significance of at least  $3\sigma$ . The same analysis is performed using peak velocity residuals, as illustrated in Figure 21 of the Appendix.

*Effect of SNR, beam size, and channel spacing*—Regardless of the signal-to-noise ratio (SNR) or angular resolution employed, line-width features are robustly detected for disc inclinations of  $-15^\circ$  and  $-30^\circ$  for the highest planet mass considered ( $q \sim 2 \times 10^{-3}$ ). Importantly, doubling the SNR at fixed beam size substantially enhances the detectability of these signatures for the lower-mass planet ( $q \sim 1 \times 10^{-3}$ ) and for the higher inclination of  $-45^\circ$ . This analysis further indicates that lower angular resolution does not necessarily hinder detectability; in some cases, it reveals features that remain undetected in higher-resolution (but lower-SNR) images and can even enhance the significance of the planet signal at larger disc inclinations.

Similarly, adopting coarser channel spacings by factors of 2–3 does not compromise the detectability of either line-width or velocity signals, as illustrated in Figures 6 and 7. However, in contrast to degrading angular resolution, the amplitudes of the planet signals remain largely unaffected until channelization effects begin to dominate. This suggests that relaxing the spectral resolution

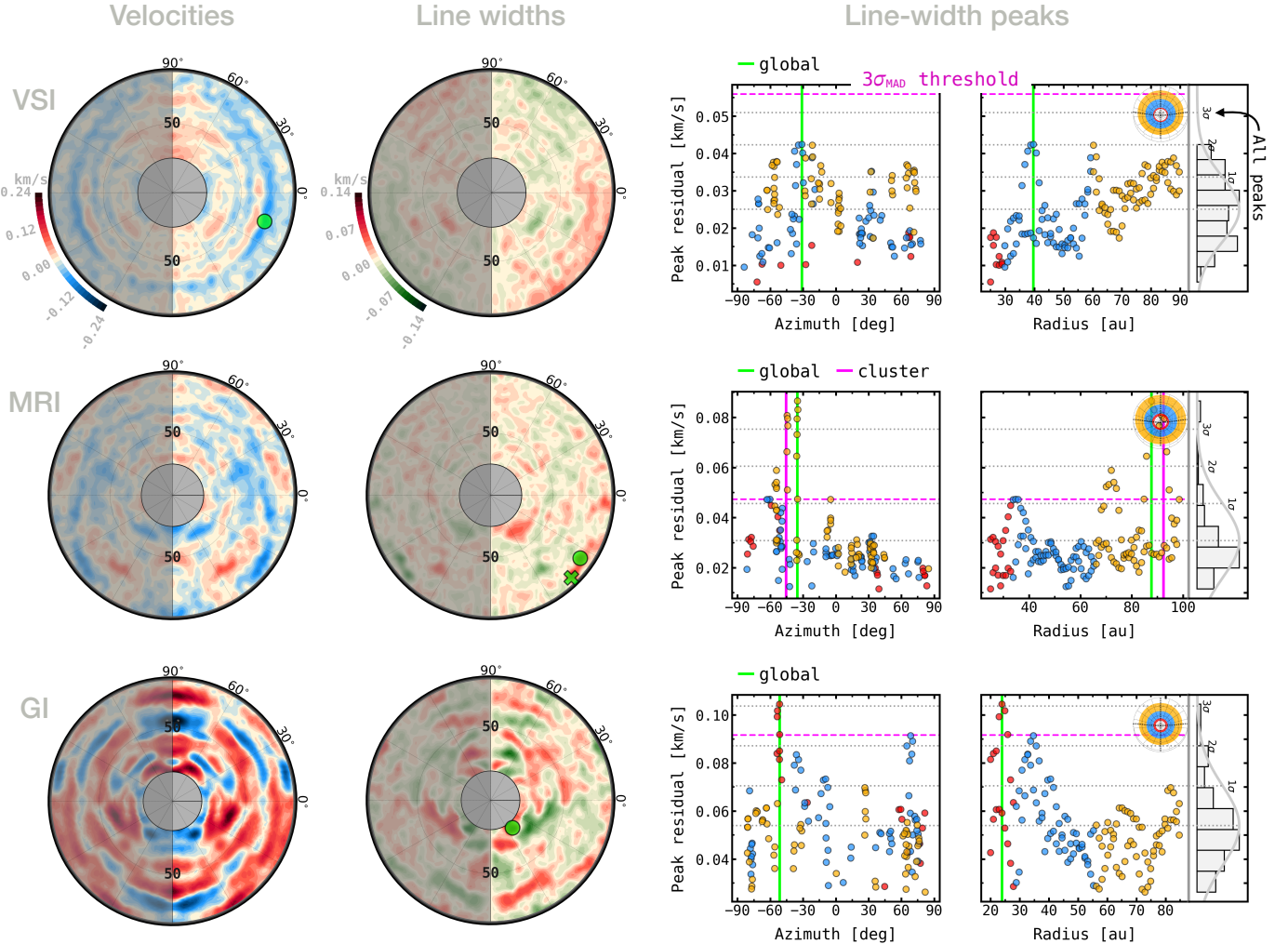


**Figure 8.** Folded velocity and line-width maps for the disc-instability simulations, showing the detected global peaks (green circles) and clusters (crosses) above the  $3\sigma$  threshold. The right-hand panels display the distribution of peak line-width residuals as a function of azimuth and radius, which are used for signal extraction and are color-coded according to the radial region of the disc from which they were derived. In Sect. 3.3, we examine the spectral origin of these signals in comparison with the planet-disc interaction scenario.

may be a viable observational alternative for boosting SNR without sacrificing planet detectability or angular resolution, particularly when probing the innermost regions of the disc where beam smearing can significantly suppress perturbations in the planet’s vicinity.

### 3.2.2. Localized signatures of disc instabilities

Although the kinematic structures produced by disc instabilities are predominantly characterized by large-scale residuals, consistent with previous studies (e.g. Hall et al. 2020 for GI; Barraza-Alfaro et al. 2021 for VSI), localized perturbations can also arise in observations of these mechanisms. This is illustrated in Figure 8, which presents folded velocity and line-width residuals together with the locations of global peaks and clusters above the  $3\sigma$  detection threshold. Among the localized

signals identified, the highest significance (in the MRI line-width maps) reaches only  $3.5\sigma$ , lower than the typical values ( $> 4\sigma$ ) obtained for the planet-disc simulation with  $q \sim 2 \times 10^{-3}$ , though comparable when the planet mass is reduced by half. Nevertheless, we do not identify complementary signatures that could plausibly mimic a planetary origin, as summarized in Fig. 20 of the Appendix. For instance, variations in the rotation velocity associated with pressure modulations, or local minima in azimuthally averaged line widths indicative of a gap, are absent at the locations of the detected features.

Crucially, we find that the morphology of the line broadening associated with the signals detected in the disc-instability models is substantially more symmetric about the line centroid than in the case of an embedded planet, indicating an intrinsic difference in the projected

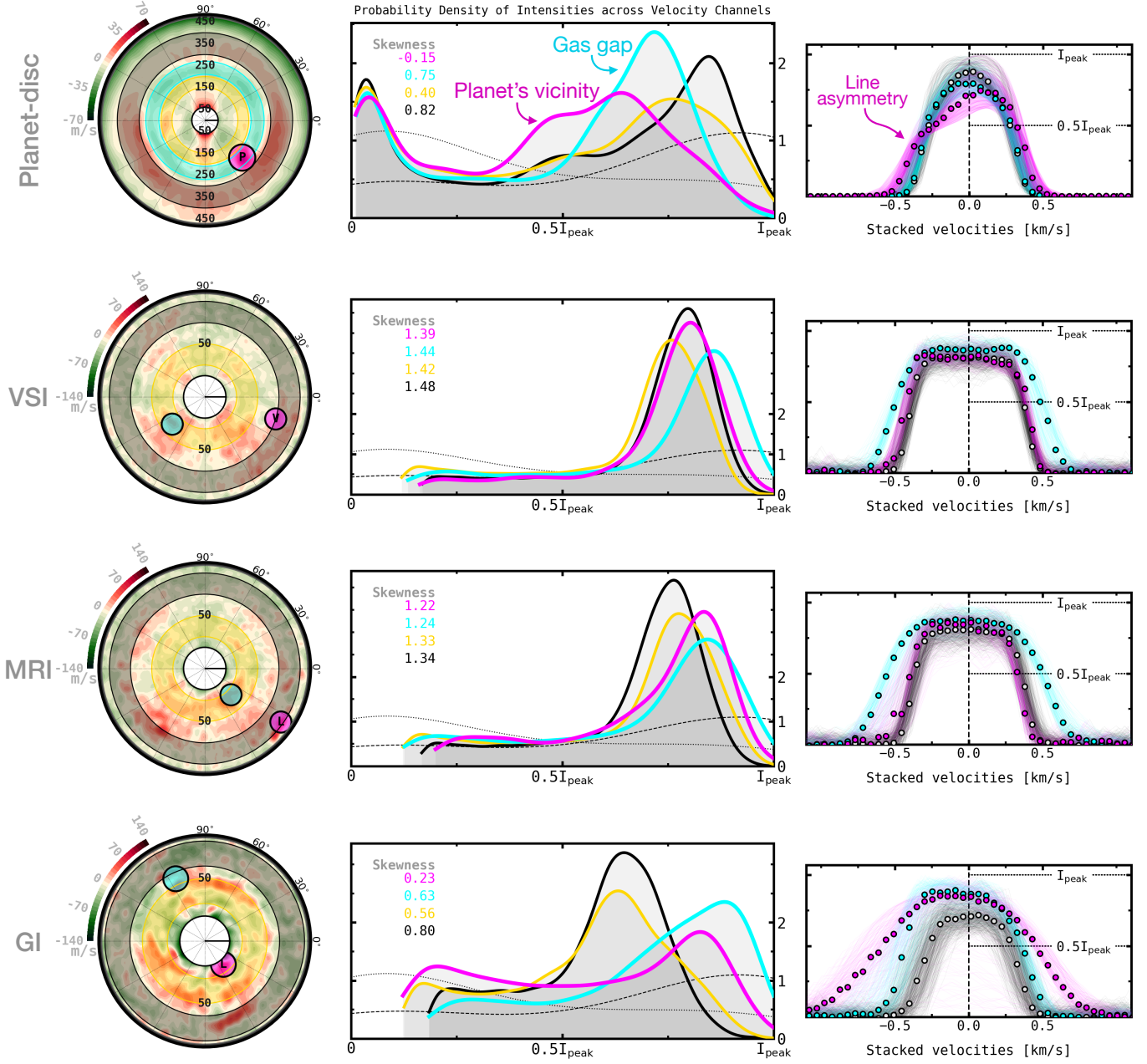


**Figure 9.** Comparison of  $^{12}\text{CO}$  intensity distributions and line-profile morphologies for the mechanisms explored in this work. The *left column* shows line-width residuals overlaid with the regions analyzed. The *middle column* presents the probability density functions of intensities from the regions highlighted on the left with the same color code, computed across all velocity channels. For reference, the dotted and dashed lines show the probability densities obtained for a Gaussian and a thick-Gaussian profile, respectively, assuming the same rms level and channel spacing of the synthetic data. In the planet-disc scenario, the magenta curve corresponds to the intensity distribution in the planet's vicinity ("P" on the left), while the blue curve traces the gap region. For the disc instabilities, the magenta curves indicate regions of enhanced line widths or velocities ("L" or "V" on the left) detected above the  $3\sigma$  threshold (in Fig. 8), while the blue curves represent other selected areas with increased line width for comparison. In all cases, the yellow and black curves represent the innermost and outermost parts of the disc. The reported skewness values are computed directly from the probability densities, with low and high values corresponding to flatter and more peaked distributions, respectively. The *right column* shows 500 randomly drawn spectra from each region, stacked in velocity after deprojection assuming Keplerian rotation. These comparisons highlight that the line broadening associated with disc instabilities is relatively isotropic, whereas planet-disc interactions produce extended tails toward low intensities and velocities, responding to the presence of high velocity gradients and coherent flows around the planet.

motions responsible for the observed line-width enhancements. As discussed in the next section, this behavior provides a robust diagnostic for distinguishing localized planet-driven signatures from substructures induced by disc instabilities.

### 3.3. *Line asymmetries and intensity distributions: planets vs. disc instabilities*

To investigate the origin of the localized features in the planet-disc and disc-instability simulations, we examine the observed intensity distributions and stacked line morphologies around the detected signals in Figure 9. The most prominent difference is that the planet-driven line broadening arises from intensity distributions that are significantly more skewed toward low intensities and blueshifted velocities than those found in quiescent regions of the disc. This pattern is consistently observed around the line-width features detected across all other planet-disc simulations, regardless of the planet azimuth, beam size, or signal-to-noise ratio. In contrast, regions of enhanced line width in disc instabilities exhibit intensity distributions centered at higher intensity values relative to other areas of the disc and show no significant asymmetries in velocity.

The pronounced line asymmetries induced by the planet in its vicinity point to intricate yet structured motions probed by the observations. They indicate that coherent velocity flows capable of producing multi-component spectra dominate in the planetary case, whereas more isotropic motions prevail in the disc instabilities. For reference, in planet-disc synthetic observations with a beam size of  $0''.3$  and a disc inclination of  $i = -15^\circ$ , we measure a blue-to-redshifted line asymmetry<sup>2</sup> of  $103 \pm 3 \text{ m s}^{-1}$  for a planet with 0.2% the mass of the star, and  $50 \pm 3 \text{ m s}^{-1}$  for a planet of 0.1%.

We attribute these asymmetries to meridional flows converging toward the planet, consistent with the velocity structure predicted by the simulations (see Fig. 22 in the Appendix). These flows are traced in the warm upper layers on the front side of the disc, where they predominantly recede relative to the observer and therefore produce a bright redshifted component in the  $^{12}\text{CO}$  line profile. In contrast, the mirrored velocity counterpart on the opposite side of the midplane (i.e. the back side) is largely suppressed by the high optical depth of the line, resulting in a deficit of blueshifted intensity. If the disc is thermally stratified, as observations systematically sug-

gest (Galloway-Sprietsma et al. 2025), this asymmetry is expected to be even more pronounced, since only gas from the colder lower layers on the back side (at velocities sampling the optically thinner line wings) can contribute to the observed blueshifted emission.

To demonstrate this behavior, we ran simulations using the optically thinner tracer  $^{13}\text{CO } J = 3 \rightarrow 2$  and extracted line profiles at the same locations for all mechanisms (see Fig. 23 in the Appendix). In the planet-disc interaction model, localized line broadening is still detected at the planet location, but the line-intensity asymmetries vanish, confirming that, in this case, converging motions from above and below the midplane contribute more equally to the observed emission. For the disc instabilities, the  $^{13}\text{CO}$  lines remain similarly symmetric about their centroids as in the  $^{12}\text{CO}$  models, indicating that the velocity fluctuations responsible for the line-width enhancements in these mechanisms are also vertically isotropic.

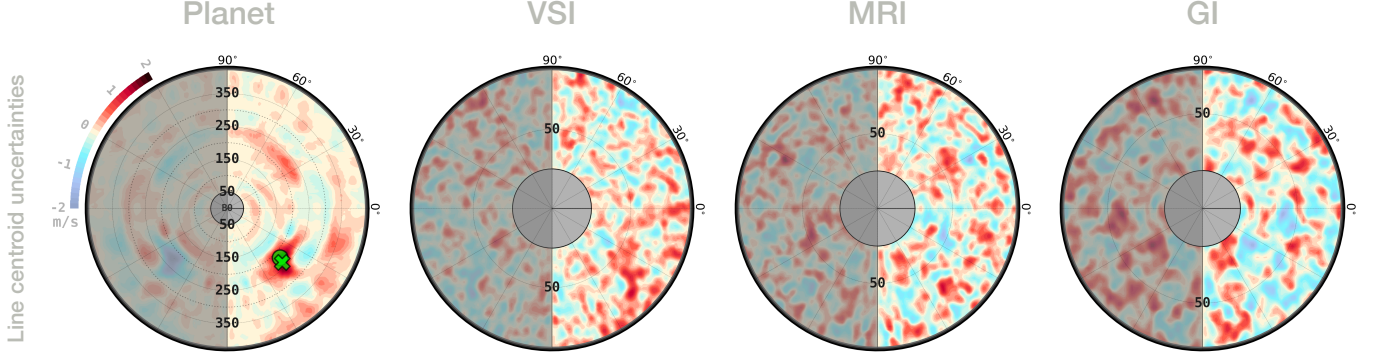
Another consequence of the velocity asymmetries induced by planets in optically thick observations is an increase in the uncertainty of the line-centroid measurements in the planet’s vicinity. As illustrated in Figure 10, this effect also produces a highly localized and clustered signal at the planet’s location, whereas for the disc-instability models, the corresponding uncertainties are distributed more broadly across the disc and show no significant correlation with the velocity or line-width substructures identified in the residual maps.

## 4. APPLICATION TO THE DISCS OF HD 135344B AND MWC 758

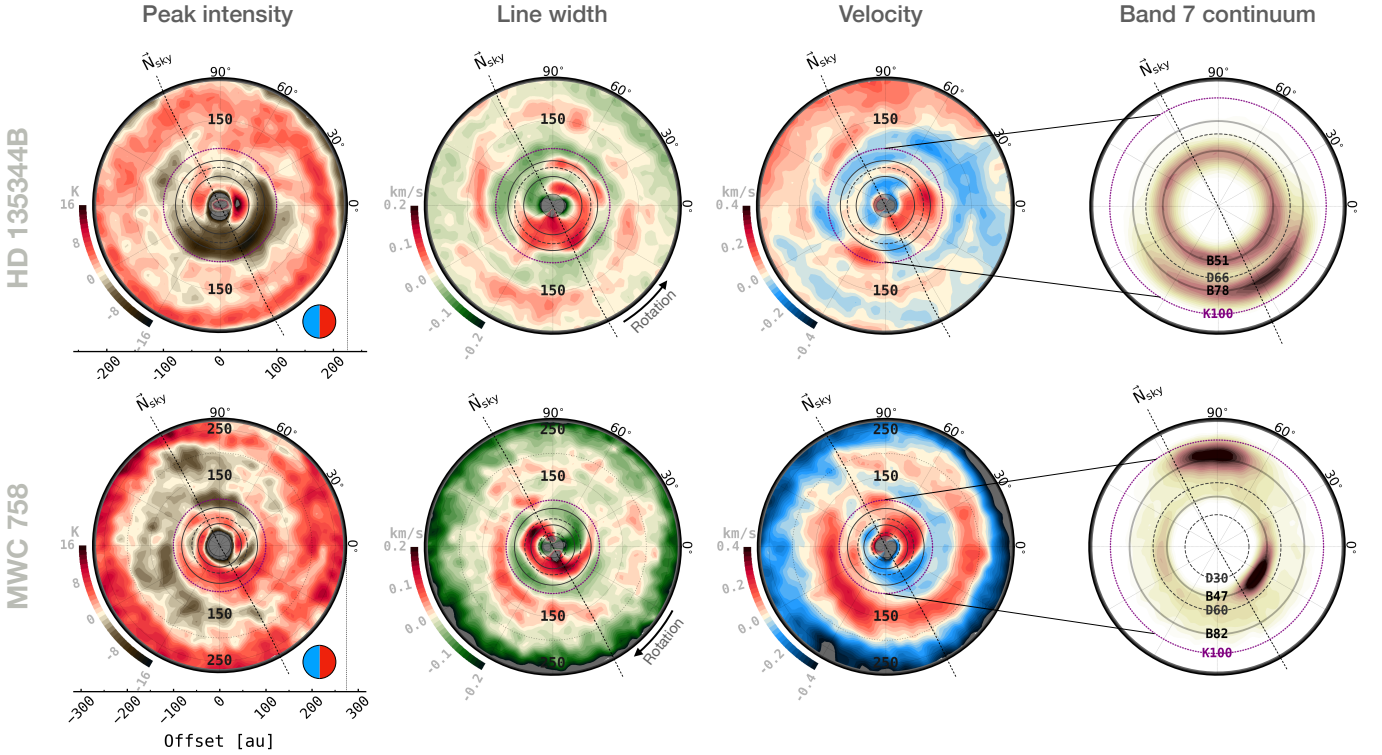
The discs of HD 135344B and MWC 758 are characterized by the presence of gaps, rings, arcs, and spiral patterns in continuum emission, potentially induced by massive yet unseen embedded planets (e.g. Garufi et al. 2013; Dong et al. 2015). Here, we apply our tomographic analysis of molecular-line data to investigate the possible planetary origin of the gas and dust structures identified in these systems.

Figure 11 presents a gallery of the residual maps derived for these sources, obtained by subtracting the best-fit DISCMINER models of the  $^{12}\text{CO } J = 3 \rightarrow 2$  line emission following Izquierdo et al. (2025). Both discs exhibit a high degree of substructure across all residual diagnostics: peak intensity, which closely traces temperature variations due to the high optical depth of the tracer; line width, which responds to surface-density and temperature fluctuations as well as unresolved velocity flows; and velocity centroids, which probe deviations from Keplerian rotation.

<sup>2</sup> Defined as the difference between the velocities at the 16th (blueshifted) and 84th (redshifted) percentiles of the line profile, computed with BETTERMOMENTS, after subtraction of the same quantity measured from the reference DISCMINER model.



**Figure 10.** Folded maps of line-centroid uncertainties extracted from the Gaussian least-squares fits to the line profiles of the planet-disc and disc-instability simulations. This quantity is computed as the square root of the absolute value of the diagonal elements of the covariance matrix returned by the fit. A localized and coherent signal is detected only around the planet’s location in this observable, resulting from the strong line asymmetries induced by the embedded planet in its vicinity, as demonstrated in Fig. 9 (top right). No strong correlation is found between these residuals and the velocity or line-width substructures observed in disc instabilities.



**Figure 11.** Peak intensity (left column), line width (middle left) and velocity (middle right) residuals traced by  $^{12}\text{CO } J = 3 \rightarrow 2$ , along with Band 7 continuum emission (right), from the discs of HD 135344B (top row) and MWC 758 (bottom), deprojected onto each disc’s reference frame. In this frame, the vertical axis is aligned with the projected minor axis of the disc on the sky. Also shown is the north axis (where PA =  $0^\circ$ ) of the sky for reference. The blue-red circle in the bottom right corner of the leftmost panels marks the blueshifted and redshifted sides of each disc. Solid and dashed lines indicate the radial location of millimeter dust rings and gaps, respectively, and the purple dotted lines highlight the orbits of the outermost planet candidates proposed in the literature to explain the observed dust features. These targets exhibit a high degree of substructure in all three types of residuals, suggesting the presence of strong pressure fluctuations and deviations from Keplerian motion.

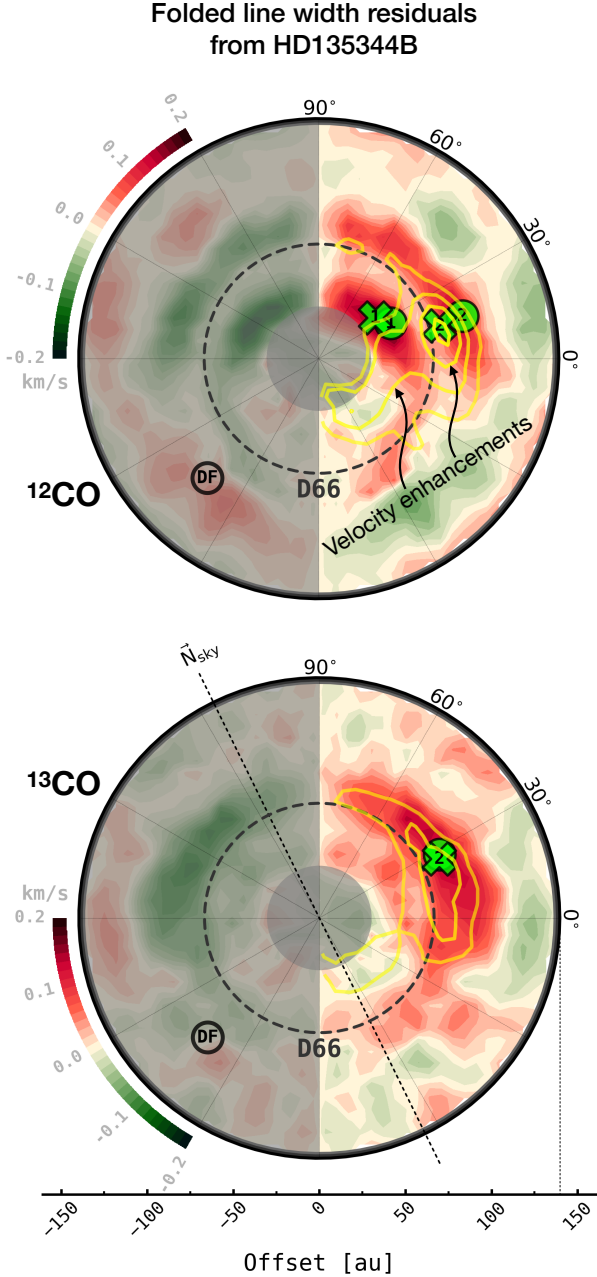


**Figure 12.** Folded line width residuals from  $^{12}\text{CO}$  and  $^{13}\text{CO}$   $J = 3 \rightarrow 2$  emission for the disc of HD 135344B. The region between  $R = 30 - 90$  au in the first quadrant displays significant line-width enhancements in both tracers, indicating perturbations spanning multiple altitudes above the disc midplane, potentially driven by a massive planet. Green circles mark the locations of global peaks, while green crosses represent detected clusters associated with highly localized signals. Yellow contours highlight co-spatial peak velocity residuals in the range of  $+50$  to  $+300$   $\text{m s}^{-1}$ . The outermost  $^{12}\text{CO}$  cluster coincides with both the global velocity peak and the detected cluster in  $^{13}\text{CO}$ .

Localized features are particularly prominent in the velocity map of HD 135344B, manifested as sharp sign reversals (or Doppler flips) that closely overlap with regions of enhanced line broadening. In contrast, MWC 758 is dominated by extended signatures, manifesting as spirals, annular structures, and arcs throughout the different line diagnostics. In the remainder of this section, we focus on the retrieval and interpretation of these features. For applications to the full exoALMA sample, we refer the reader to Fukagawa et al. (2026) and Benisty et al. (2026), which present a systematic identification and analysis of residuals across all targets.

#### 4.1. Localized features in HD 135344B

We follow the approach described in Section 3.2 to search for planet candidates associated with localized signatures in the line-width and velocity maps of HD 135344B. In this source, we identify strongly localized line-width peaks and clusters, shown in Figure 12 as circles and crosses, respectively. Two such features, labeled “1” and “2”, are detected in  $^{12}\text{CO}$  at ( $R = 41$  au,  $\phi = 36^\circ$ ) and ( $R = 73$  au,  $\phi = 15^\circ$ ), and in  $^{13}\text{CO}$  at ( $R = 78$  au,  $\phi = 26^\circ$ ), where  $R$  denotes the cylindrical radius and  $\phi$  is the azimuthal angle measured from the redshifted major axis in the deprojected disc frame. Although these features dominate the peak extraction, line-width enhancements in  $^{12}\text{CO}$  are also observed near the velocity Doppler flip labeled “DF”, reported in Sect. 4.1.1 at ( $R = 95$  au,  $\phi = -133^\circ$ ). Table 1 summarizes the locations of these planet candidates, together with their sky-projected coordinates relative to the disc center from the best-fit DISCMINER model of Izquierdo et al. (2025).

The amplitudes of the detected line-width signals in  $^{12}\text{CO}$  are  $0.18$  and  $0.13$   $\text{km s}^{-1}$  for candidates “1” and “2”, respectively, and  $0.16$   $\text{km s}^{-1}$  for the  $^{13}\text{CO}$  feature associated with candidate “2”. Prominent velocity residuals are also found in the same region of the disc (shown as yellow contours), reaching amplitudes of up to  $0.26$   $\text{km s}^{-1}$  in  $^{12}\text{CO}$ , and  $0.14$   $\text{km s}^{-1}$  in  $^{13}\text{CO}$ . However, these residuals do not form clusters that are significantly more localized than those observed elsewhere in the disc, indicating that velocity perturbations are spatially more extended than the corresponding line-width enhancements. This behavior is fully consistent with the predictions from our massive planet-disc interaction simulations analysed in Sect. 3 (see e.g. Fig. 3).

Izquierdo et al. (2023) reported similar localized line broadening traced by CO emission in the disc of HD 163296, spatially coincident with a planet candidate associated with a velocity Doppler flip and chemical anomalies attributed to its circumplanetary region

**Table 1.** Planet candidates identified in the disc of HD135344B, including their locations in polar and sky-projected coordinates.

Candidate	$R$ [au]	$\phi$ [°]	$R$ ["]	PA [°]	Tracer
C1	41	36	0.30	278	$^{12}\text{CO}$
C2	73	15	0.54	258	$^{12}\text{CO}$ & $^{13}\text{CO}$
DF	95	-133	0.69	109	$^{12}\text{CO}$ & $^{13}\text{CO}$

(Izquierdo et al. 2022, 2026); in the disc of MWC 480, at the radial location of candidate planet-driven buoyancy spirals (Teague et al. 2021); and in AS 209, in the region where a circumplanetary disc was proposed based on localized  $^{13}\text{CO}$  intensity signals (Bae et al. 2022).

#### 4.1.1. A prominent Doppler flip at $R=95$ au

Doppler-flip signatures also serve as indicators of the presence of embedded planets in discs. These features manifest as sharp transitions between negative and positive velocity residuals, arising from the gravitational interaction between the planet and the surrounding gas in its vicinity (e.g. Pérez et al. 2018). They also provide valuable diagnostics of the planet mass and orbital parameters and, to a lesser extent, of the local disc viscosity and temperature structure (Rabago & Zhu 2021).

In cases with high substructure complexity, where Doppler-flip perturbations are not the strongest but remain visually detectable as in the disc of HD 135344B, we apply a peak-finding algorithm on gradient residual maps to pinpoint the central location of these signatures. This is illustrated in Figure 24 of the Appendix, where we present azimuthal gradient maps of velocity residuals in  $^{12}\text{CO}$  and  $^{13}\text{CO}$ . Pluses and minuses overlaid on the reference residual map denote positive and negative peak gradients, respectively, to mark the locations of Doppler flips in the velocity field. Azimuthal gradient peaks with values below  $50 \text{ m s}^{-1} \text{ beam}^{-1}$  were excluded from the analysis, retaining only the steepest gradients corresponding to velocity shifts exceeding half the channel spacing of the data per beam. The radial section of the disc where the Doppler-flip signatures overlap in  $^{12}\text{CO}$  and  $^{13}\text{CO}$  is highlighted. Among the peaks that are co-spatial within a beam size ( $\sim 20$  au at the source distance) for these tracers, three correspond to sequential velocity sign flips centered at  $(R, \phi) = (95 \text{ au}, -133^\circ)$ ,  $(89 \text{ au}, -93^\circ)$ , and  $(80 \text{ au}, -60^\circ)$  in the disc reference frame, and one at  $(72 \text{ au}, 24^\circ)$  co-spatial with the line-width clusters and velocity perturbations reported earlier in Fig. 12.

We propose the presence of a massive embedded planet at the location of the most prominent Doppler flip, centered at  $R = 95$  au and  $\phi = -133^\circ$ . The

peak negative-to-positive amplitude of this signal is  $0.32 \pm 0.02 \text{ km s}^{-1}$  in  $^{12}\text{CO}$  and  $0.24 \pm 0.04 \text{ km s}^{-1}$  in  $^{13}\text{CO}$ , implying a modest decrease toward the disc midplane. Additional evidence supporting this candidate includes a spiral-like structure seen in positive line-width residuals (Figs. 11 and 12, top row) emerging from the location of the Doppler flip, as well as a local minimum in the azimuthally averaged line widths at this orbital separation (Fig. 10 in Izquierdo et al. 2025), which may indicate a surface-density gap traced by reduced line saturation owing to the lower optical depth (Hacar et al. 2016; Izquierdo et al. 2021).

Variations in the amplitude of this velocity feature across lines may provide additional clues about the vertical location and physical mechanism driving the signal. Given that the disc of HD 135344B is close to face-on ( $i = -16^\circ$ ), we speculate that a substantial fraction of the observed velocity signals, and their modulation with altitude, are likely shaped by vertical motions. Pinte et al. (2019) and Rabago & Zhu (2021) found in their simulations that vertical downward velocities are highest near an embedded planet peak at approximately one pressure scale height above the midplane. In our proposed scenario, this would imply that  $^{12}\text{CO}$  traces gas closer to this elevation than  $^{13}\text{CO}$ , suggesting a relatively flat disc compared to the average  $z/r$  of the exoALMA sample. Interestingly, this interpretation is consistent with the low  $z/r$  values reported for discs with similar radial extents, such as CQ Tau or PDS 66 (see e.g. Fig. 6 of Galloway-Sprietsma et al. 2025). The assumption of a shallow disc to explain the reduction in velocity amplitude toward the midplane could be relaxed, however, if the planet also excites buoyancy resonances. In that case, vertical motions would begin to weaken from even higher elevations (Bae et al. 2021).

To further investigate the influence of this planet on the disc structure, we generated a velocity map from hydrodynamical models of planet-disc interaction tailored to this system using the PPDONET neural network (Mao et al. 2023). We then subtracted the best-fit Keplerian rotation derived with DISCMINER for this target in Izquierdo et al. (2025) to obtain velocity residuals. The adopted setup assumes a gas-disc alpha viscosity of  $10^{-2}$ , an aspect ratio of 0.075, and a  $6 M_{\text{Jup}}$  planet located at the center of the Doppler flip<sup>3</sup>, consistent with

<sup>3</sup> These parameters were not derived from a formal best-fit procedure but were manually adjusted to qualitatively reproduce the localized and large-scale features observed in the data. Moreover, because the neural network does not account for vertical motions or vertically stratified temperature structures, the adopted parameters may not correspond to the optimal physical properties required to reproduce the observed disc kinematics.

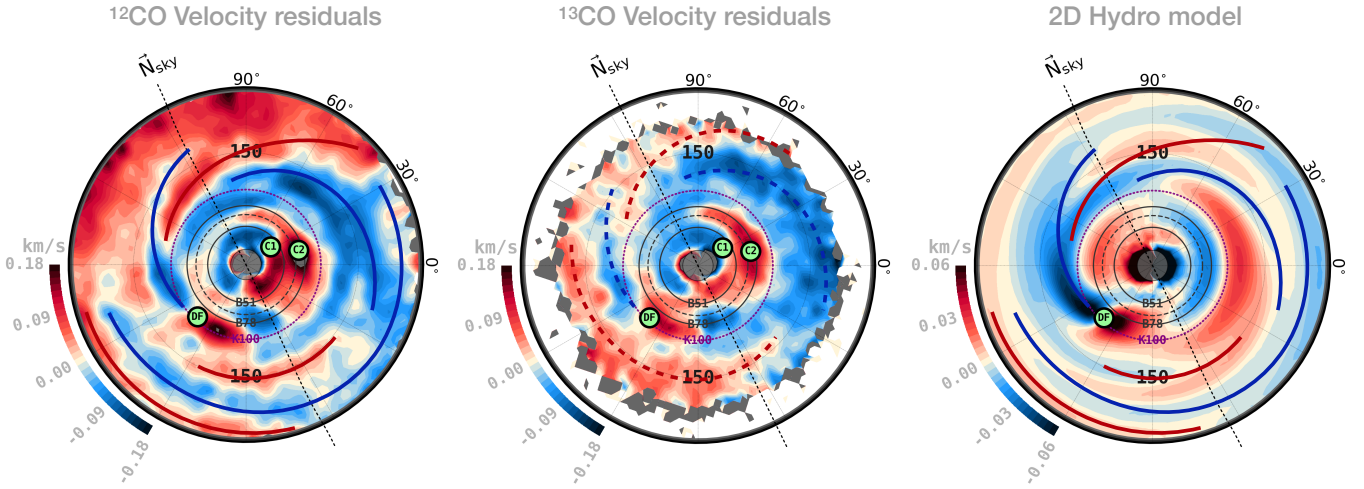


**Figure 13.** Centroid velocity residuals observed in the  $^{12}\text{CO}$  and  $^{13}\text{CO}$  data of the HD 135344B disc, compared with a two-dimensional hydrodynamical model tailored to this system. The Doppler flip identified in Sect. 4.1.1, centered at the DF marker, spatially overlaps in both tracers and is accompanied by large-scale velocity substructures spanning a broad radial and azimuthal extent of the disc. These features are qualitatively reproduced by the hydrodynamical model, generated with the PPDONET neural network introduced by Mao et al. (2023) and postprocessed with DISCMINER, assuming a  $6 M_{\text{Jup}}$  planet at the center of the Doppler flip, an aspect ratio of 0.075, and an  $\alpha$  viscosity of  $10^{-2}$ . The red and blue solid lines overlaid on the model residuals trace the large-scale  $^{12}\text{CO}$  signatures, emphasizing the similarity in both the velocity sign flips and the spatial extent of the structures near and far from the planet, despite the simplicity of the adopted model.

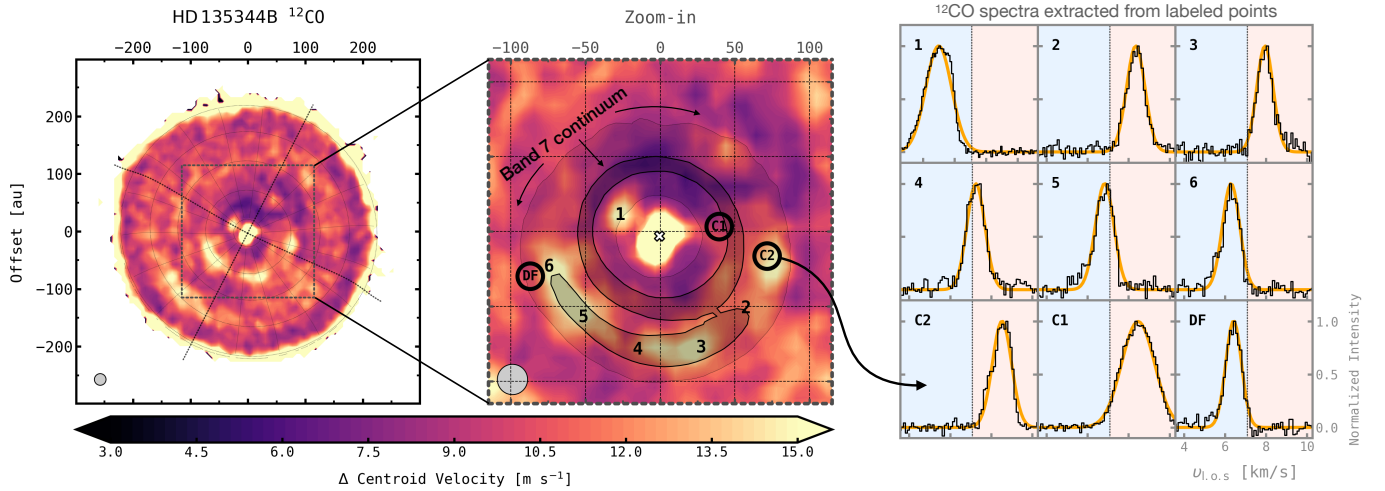


**Figure 14.** Statistical uncertainties in centroid velocities derived from Gaussian fits to the  $^{12}\text{CO}$   $J = 3 \rightarrow 2$  line profiles for the disc of HD 135344B. The zoom-in panel highlights localized signals near the mm continuum crescent (outlined by black contours to the south), around the proposed planet associated with line-width clusters and velocity peaks at  $R = 73$  au (denoted by the C2 circle), and near the planet candidate linked to the velocity Doppler-flip signature at  $R = 95$  au (marked by the DF circle). In the rightmost panels, spectra extracted from the numbered points in the middle panel illustrate the asymmetric line profiles responsible for the increased uncertainties. These morphologies suggest the presence of spatially unresolved velocity flows and are reminiscent of the line shapes predicted by synthetic observations of planet-disc interaction simulations (see Sect. 3.3).

previous models used to reproduce the spiral arms observed in scattered light (see Sect. 5.1 for discussion).

Figure 13 compares the residuals from the  $^{12}\text{CO}$  and  $^{13}\text{CO}$  data with those predicted by the hydrodynamical model. In addition to the Doppler flip signature, the model exhibits large-scale substructures including arcs and spiral-like patterns, that closely resemble those observed in  $^{12}\text{CO}$  (traced by the solid blue and red lines) and in  $^{13}\text{CO}$ . The consistency of the velocity patterns across different molecular lines suggests that the observed substructures share a common origin and that the associated perturbations propagate over multiple scale heights within the disc’s vertical structure.

We note, however, that although the overall dynamical structure of the disc is well reproduced by invoking this planet, the amplitude of the model residuals is lower by a factor of  $\sim 2-3$  compared to the observations. This discrepancy may be mitigated by incorporating vertical motions and temperature gradients into the models, which are expected to enhance the planet-driven velocity features (e.g. Bae et al. 2021) without requiring a prohibitively high planet mass that would otherwise conflict with direct-imaging constraints ruling out planets more massive than  $3 M_{\text{Jup}}$  at the orbital radius of the Doppler Flip (Cugno et al. 2024). Full three-dimensional simulations are therefore essential to reliably constrain the masses of embedded planets from kinematic signatures, particularly in low-inclination discs.

#### 4.1.2. Line asymmetries around line-width signals

We also find evidence for asymmetric line profiles at the locations of the outermost line width clusters detected in  $^{12}\text{CO}$  and  $^{13}\text{CO}$ , consistent with the predictions from our planet-disc interaction simulations discussed in Sect. 3.3. Figure 14 presents a map of  $1\sigma$  statistical uncertainties in centroid velocities derived from Gaussian fits to the  $^{12}\text{CO}$  line emission of this source. Typical uncertainties are  $\sim 10 \text{ m s}^{-1}$ , with enhanced values partially tracing the millimeter continuum crescent and localized increases around the line-width cluster at  $R = 73 \text{ au}$  and near the Doppler Flip identified at  $R = 95 \text{ au}$ . An additional localized feature is found interior to the millimeter ring B51, at  $R = 30 \text{ au}$ .

To illustrate the origin of these elevated uncertainties, we extracted spectra at the positions of the outer line-width cluster and at pixels co-spatial with the millimeter crescent. These profiles exhibit clear asymmetries relative to their line centroids and, in the most prominent cases, appear double-peaked, indicating the presence of multiple overlapping velocity components. In all cases, however, the asymmetries favor downward flows, consistent with predictions from our planet-disc simulations

(see Figs. 9 and 22). Near the outer edge of the disc, at  $R \sim 170 \text{ au}$ , elevated uncertainties also align with the spiral structure identified in line-width residuals (Fig. 11), suggesting spatially unresolved and asymmetric velocity flows along this feature as well.

Figure 15 summarizes the localized signatures identified in HD 135344B. In Section 5, we examine the possible connection between these candidate planet-driven perturbations and the dust substructures revealed by millimeter and near-infrared continuum observations of this source.

#### 4.2. Large-scale signatures in MWC 758

The disc of MWC 758 exhibits prominent spiral-like signatures across all three residual diagnostics. To identify and quantify these perturbations, we employ the FILFINDER code (Koch & Rosolowsky 2015), which applies an adaptive thresholding algorithm to isolate pixels belonging to coherent substructures (referred to as filaments) over a wide dynamic range in the observable of interest. Each detected substructure is assigned a two-dimensional mask, which is subsequently reduced to a one-dimensional skeleton via a Medial Axis Transform (first introduced by Blum 1967) to serve as a shape descriptor. The resulting medial axes are then used to characterize the morphology and spatial configuration of the filaments (see e.g. Izquierdo et al. 2022, for an application to the disc kinematics of HD 163296). For this purpose, we consider several geometric descriptors provided by FILFINDER, including filament length, width, and orientation.

**Table 2.** Best-fit parameters for the logarithmic and linear spiral prescriptions fitted to the velocity structures traced by  $^{12}\text{CO } J = 3 \rightarrow 2$  emission in the disc of MWC 758. The parameter  $b$  in the linear fit is expressed in units of  $\text{au rad}^{-1}$ .

Type	Component	$a$ (au)	$b$
Logarithmic ( $r = ae^{b\phi}$ )	Positive	$170.0 \pm 1.1$	$5.5 \pm 0.3^\circ$
	Negative	$95.8 \pm 2.3$	$15.1 \pm 1.4^\circ$
Linear ( $r = a + b\phi$ )	Positive	$171.7 \pm 1.1$	$15.8 \pm 0.6$
	Negative	$99.4 \pm 1.9$	$26.2 \pm 1.7$

The results of this analysis are presented in Figure 25 in the Appendix, which shows the filaments identified in the  $^{12}\text{CO}$  velocity residuals, together with their measured pitch angles and projected widths. We find that the longest velocity feature, highlighted in cyan across all panels, exhibits a nearly uniform pitch angle of  $\sim 0.3^\circ$  at all radii, forming an annular pattern that coherently traces blueshifted velocities consistent with outflowing material in the outer disc regions (see Benisty et al.

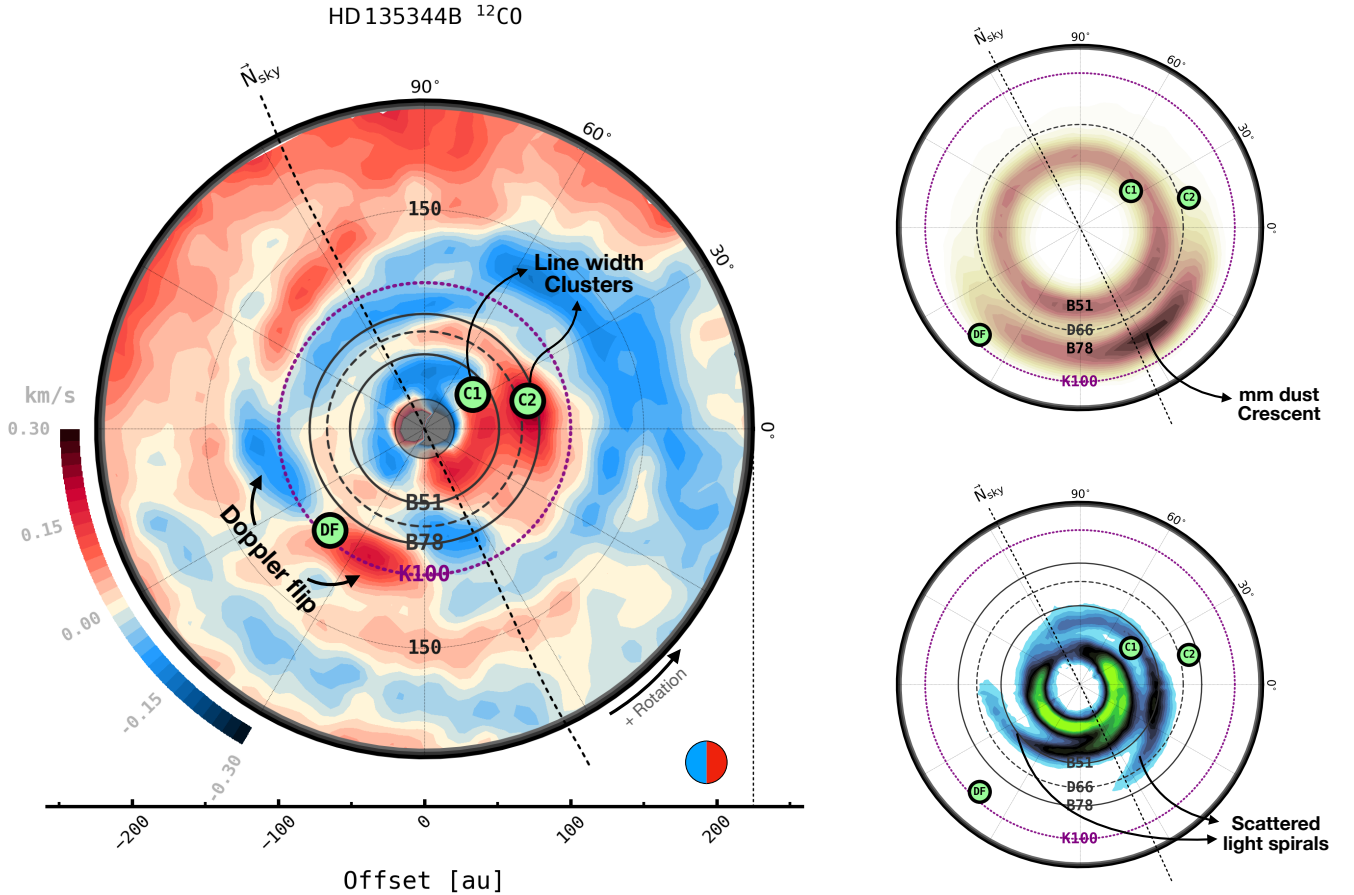


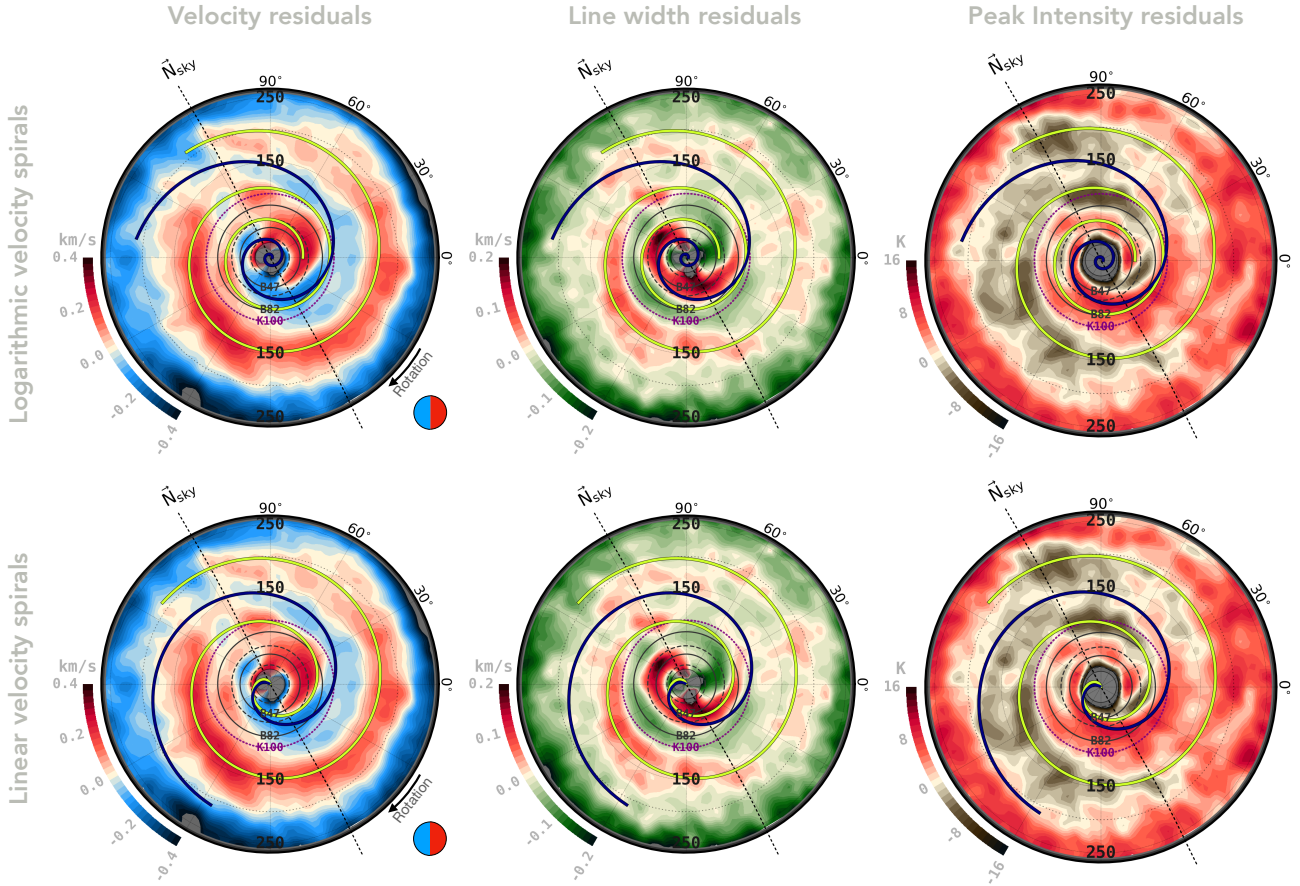
**Figure 15.** Deprojected view of velocity and dust substructures in the disc of HD 135344B. *Left:*  $^{12}\text{CO } J = 3 \rightarrow 2$  velocity residuals illustrating deviations from Keplerian rotation in the gas disc. *Bottom right:* VLT/SPHERE near-infrared observations (Stolker et al. 2016) probing scattered light from micron-sized dust grains. *Top right:* ALMA Band 7 continuum observations (Teague et al. 2025; Curone et al. 2025) tracing thermal emission from millimeter-sized dust grains. Solid and dashed lines mark the radial locations of peaks and troughs in the millimeter continuum, while the purple dotted K100 line indicates the orbital radius of the planet candidate proposed by Dong et al. (2015) and Bae et al. (2016) to reproduce the near-infrared spirals and the millimeter dust crescent. The green circles indicate the locations of the Doppler flip and line-width clusters identified in  $^{12}\text{CO}$  and  $^{13}\text{CO}$  in this work, potentially associated with embedded planets.

2026, for details). In contrast, the larger and radially varying pitch angles retrieved for the inner filaments suggest that these correspond to non-axisymmetric substructures forming spiral patterns, possibly driven by embedded companions (see Sect. 5). We also find that the two outermost filaments are spatially resolved, with an average full width at half maximum of  $\sim 1.5$  beams measured perpendicular to their medial axes. The outermost blueshifted filament, however, may extend beyond this width in regions of lower signal-to-noise that were excluded from the analysis.

The velocity spirals manifest as coherent redshifted and blueshifted patterns extending over more than  $\sim 270^\circ$  in azimuth, without sign reversals across the disc’s minor and major axes. As illustrated in Fig. 2, this behavior suggests that the signatures are likely dominated by downward and upward vertical motions, respectively.

To further characterize the morphology of these substructures, we fitted logarithmic ( $r = ae^{b\phi}$ ) and linear ( $r = a + b\phi$ ) spiral models to their medial axes using SCIPY’s least-squares minimization algorithm. Figure 16 shows the resulting analytic spirals overlaid on the velocity, line-width, and peak-intensity residual maps, with the best-fit parameters listed in Table 2. Both logarithmic and linear prescriptions reproduce the overall geometry of the velocity spirals reasonably well. However, the extrapolated logarithmic spiral provides a better match to velocity and intensity features in the inner disc, particularly near the millimeter dust crescents B47 and B82, which the linear model fails to capture.

This analysis also demonstrates that the redshifted velocity spiral spatially coincides with elongated regions of enhanced line width, regardless of the adopted fitting prescription. The absence of corresponding tempera-

MWC 758  $^{12}\text{CO}$ 

**Figure 16.** Logarithmic ( $r = ae^{b\phi}$ , top) and linear ( $r = a + b\phi$ , bottom) spiral models fitted to the spirals identified in  $^{12}\text{CO}$  velocity residuals for the disc of MWC 758, overlaid on the velocity (left), line-width (middle), and peak-intensity (right) residual maps. Table 2 summarizes the best-fit parameters for the spirals. While both prescriptions reproduce the overall morphology of the outer signatures in velocity and line width, the logarithmic model additionally captures the inner features in velocity and peak intensity near the radial locations of the millimeter dust crescents B47 and B82.

ture increases along this spiral, as traced by the  $^{12}\text{CO}$  peak intensity residuals, indicates that the observed line broadening most likely arises from unresolved velocity flows, high optical depths, or a combination of both, rather than from shock or radiative heating of the gas.

## 5. DISCUSSION

### 5.1. Planets in the disc of HD 135344B

As illustrated in Figure 15, all kinematic and line-width signatures identified in the disc of HD 135344B are located near the dust ring (B51), gap (D66), and azimuthal dust trap (B78) observed in the millimeter continuum (van der Marel et al. 2016; Cazzoletti et al. 2018; Curone et al. 2025), suggesting a strong connection between these substructures and pressure modulations potentially induced by embedded companions. Notably, the same radial region of the disc hosts a nearly symmetric two-armed spiral structure observed in the near

infrared (Muto et al. 2012; Garufi et al. 2013; Stolker et al. 2016; Ren et al. 2023; Maio et al. 2025), consistent with expectations from tidal interactions between discs and planets (e.g. Dong et al. 2015; Bae et al. 2016; Baruteau et al. 2019). From a kinematic perspective, and based on the small and large-scale signatures identified in Sect. 4.1, we propose three plausible locations for embedded planets in this disc.

First, a planet candidate (C2) at a radial separation of  $R = 73$  au, near the inner edge of the millimeter dust asymmetry B78 and azimuthally within the first half of the first quadrant of the disc, centered at  $\phi = 15^\circ$  as inferred by our clustering analysis (or  $R = 0''.54$ , PA =  $258^\circ$  in projected sky coordinates). This object would produce line broadening and blueshifted asymmetries, as well as strong velocity perturbations at different heights above the midplane traced by  $^{12}\text{CO}$  and  $^{13}\text{CO}$  (Figs. 12, 13, and 14). Its radial location is close to that of

the planet proposed by Xie et al. (2024) at an orbital radius of  $R = 66$  au to explain the pattern speed of the near-infrared spirals<sup>4</sup> observed in this source (Fig. 15).

The second candidate (C1) corresponds to a closer-in planet located at  $R = 41$  au and  $\phi = 36^\circ$  (or  $R = 0''.30$ , PA =  $278^\circ$ ), interior to the inner dust ring B47, and possibly responsible for the localized line broadening in the disc upper layers traced by  $^{12}\text{CO}$  (Fig. 12). However, the absence of  $^{12}\text{CO}$  line asymmetries (Fig. 14) and the only moderate broadening detected in  $^{13}\text{CO}$  at this location suggest that, if such a planet exists, it is likely less massive than  $1.6 M_{\text{Jup}}$  (i.e.  $< 0.1\%$  of the stellar mass), as predicted by our planet-disc interaction models. Alternatively, these signatures may reflect outlier perturbations from an even more interior planet that cannot be robustly constrained due to beam smearing at small radii, given the finite angular resolution of our data ( $\sim 20$  au at the source distance). This scenario would be broadly consistent with the findings of Maio et al. (2025), who propose a  $2 M_{\text{Jup}}$  planet to explain a compact infrared intensity signal at an orbital radius of 29 au and an azimuth of  $\phi = 31^\circ$ , which overlaps in azimuth with the  $^{12}\text{CO}$  line-width feature reported here, though at a slightly smaller radial separation.

This also aligns with Garufi et al. (2013) and van der Marel et al. (2016), who suggested that a massive planet at  $\sim 30$  au could generate the pressure maximum responsible for the millimeter dust ring B51. van der Marel et al. (2016) further proposed that this inner pressure bump could induce a secondary pressure maximum at larger radii, triggering a vortex via the Rossby wave instability and leading to the formation of the millimeter dust crescent B78 as an asymmetric dust trap. In their interpretation, one of the spiral arms observed in scattered light would originate from the vortex overdensity, while the other would be driven by the inner planet candidate. Interestingly, Cazzoletti et al. (2018) argued that the vortex alone could potentially excite the entire spiral structure, having accumulated sufficient mass (up to a few Jupiter masses) to perturb the disc kinematics. Such a scenario could account for the enhanced line widths (Fig. 11) and spectral asymmetries (Fig. 14) observed around the dust crescent. This is also partly consistent with the findings of Wölfer et al. (2025), who show that the kinematic pattern near the millimeter crescent resembles that expected from a vor-

tex, although it cannot, on its own, reproduce the more extended features.

Finally, we identify a third planet candidate (DF) associated with a Doppler-flip velocity signature in the third quadrant of the disc at  $R = 95$  au and  $\phi = -133^\circ$  (or  $R = 0''.69$ , PA =  $109^\circ$ ), detected in both  $^{12}\text{CO}$  and  $^{13}\text{CO}$  velocity maps. This planet may also be responsible for a surface-density dip traced by reduced azimuthally averaged line widths at the same orbital radius (see Fig. 10 of Izquierdo et al. 2025, and Fig. 20 of this work). Moreover, its inferred location is in excellent agreement with the planet proposed by Dong et al. (2015) and Bae et al. (2016) to explain both the two-armed spiral observed in scattered light and the millimeter dust crescent B78.

Notably, this Doppler flip is intersected by the innermost tip of a large-scale line-width spiral extending between  $\sim 100$ -200 au (see Fig. 11, top row), and may therefore be associated with the spiral density waves driven by the planet. The absence of elevated temperatures along this spiral further suggests a non-thermal origin, likely associated with enhanced turbulence, or more generally, unresolved velocity flows, increased optical depth, or a combination of both. This complements the findings of Casassus et al. (2021), who reported turbulent spiral features traced by  $^{12}\text{CO } J = 2 \rightarrow 1$  emission in this source, albeit located closer to the inner disc and spatially coincident with the near-infrared spirals.

## 5.2. Origin of the spirals structures in MWC 758

Previous studies of the disc around MWC 758 have revealed spiral structures traced by scattered light (Grady et al. 2013; Benisty et al. 2015) and molecular line emission (Boehler et al. 2018), as well as pronounced asymmetries in the millimeter continuum (Dong et al. 2018) within the inner  $\sim 100$  au. From a kinematic perspective, this source stands out within our sample due to its prominent velocity and line width spirals, which extend from the inner disc regions out to  $\sim 200$  au in both  $^{12}\text{CO}$  and  $^{13}\text{CO}$  lines. Figure 17 illustrates the spatial configuration of these velocity substructures together with the near-infrared spirals and the locations of the millimeter continuum crescents.

Two main scenarios involving embedded companions have been proposed to explain the origin of the continuum substructures in this source. The first invoke the presence of at least one massive planet or stellar companion inside the millimeter dust cavity ( $R_p < 49$  au), with the near-infrared two-armed spirals located exterior to the companion's orbit. The second scenario proposes a massive planet outside the cavity, capable of exciting the spirals interior to its orbit.

<sup>4</sup> The reference Keplerian velocity adopted in the spiral-pattern analysis is consistent with that used in this work, as Xie et al. (2024) assumed a nearly identical stellar mass ( $1.6 M_\odot$ ) and disc inclination ( $16.7^\circ$ ), matching the values independently inferred from the disc kinematics in Izquierdo et al. (2025).

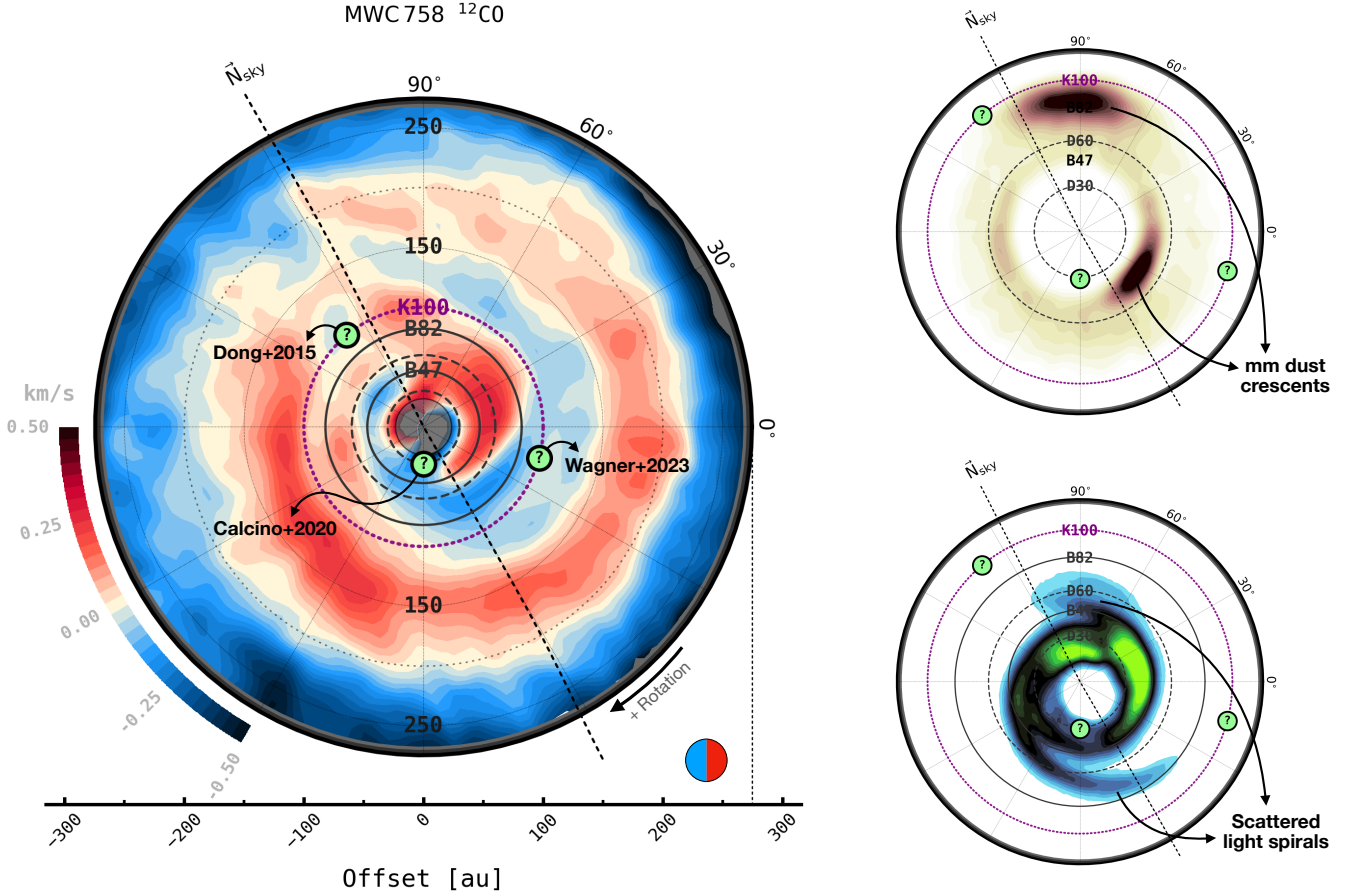


**Figure 17.** Deprojected view of velocity and dust substructures in the disc of MWC 758. *Left:*  $^{12}\text{CO } J = 3 \rightarrow 2$  velocity residuals illustrating deviations from Keplerian rotation in the gas disc. *Bottom right:* VLT/SPHERE near-infrared observations (Benisty et al. 2015) probing scattered light from micron-sized dust grains. *Top right:* ALMA Band 7 continuum observations (Teague et al. 2025; Curone et al. 2025) tracing thermal emission from millimeter-sized dust grains. Solid and dashed lines mark the radial locations of peaks and troughs in the millimeter continuum, while the purple dotted K100 line indicates the orbital radius of the giant planet proposed by Wagner et al. (2023) based on a compact signal identified at infrared wavelengths. The green circles indicate the locations of selected planet candidates reported in the literature to explain the observed dust substructures.

Within the first group, Calcino et al. (2020) showed that a massive planet on an eccentric orbit ( $e = 0.4$ ) with a semi-major axis of 33.5 au—close to the point-like source reported by Reggiani et al. (2018) at  $\sim 20$  au—can independently reproduce the two-armed spiral structure. In the second group, Dong et al. (2015) demonstrated that a single massive planet ( $M_p/M_\star = 6 \times 10^{-3}$ ) located at  $R_p \sim 100$  au could similarly excite the observed spirals. More recently, Wagner et al. (2023) reported a localized infrared intensity signal at a similar orbital radius, though on the opposite side of the disc, spatially connected to the southern near-infrared spiral arm. While such a planet would be broadly consistent with the line-width minimum identified in our data after azimuthal averaging at  $R \sim 90$  au, the absence of a localized velocity or line-width perturbation at this orbital radius disfavors the presence of a high-mass companion.

By measuring the pattern speed of the near-infrared spirals, Ren et al. (2020) also proposed the presence of an outer planet, though at a larger orbital radius of 172 au. Since that study adopted higher values for both the stellar mass and disc inclination ( $M_\star = 1.9 M_\odot$  and  $i = 21^\circ$ ) than those inferred from our kinematic analysis ( $M_\star = 1.4 M_\odot$  and  $i = 19.4^\circ$ ; Izquierdo et al. 2025), the corresponding planet location would shift to smaller radii when recalculated using our updated parameters. Similarly, the absence of localized perturbations in these outer regions argues against the presence of a high-mass planet at such separations.

Turning to the kinematical features revealed in our data, vertical motions appear to play a dominant role in shaping the tightly wound velocity spirals observed in this source (Fig. 17). This effect is likely enhanced by the nearly face-on orientation of the disc, in which radial and azimuthal velocity components are strongly

suppressed by projection effects. If these spirals are of planetary origin and intrinsically dominated by vertical motions, their morphology and velocity structure would be broadly consistent with spiral waves launched at buoyancy resonances by an embedded companion (Bae et al. 2021). Spirals driven at Lindblad resonances by an inner massive planet could, in principle, account for the large pitch angles traced by the scattered light spirals in the inner disc, while also reproducing the gradual decrease in pitch angle of the outer velocity spirals with radius ( $< 10^\circ$ , see Fig. 25). Alternatively, a hybrid scenario involving at least one inner massive planet ( $R_p < 40$  au) responsible for the large-pitch spirals in the inner disc, and an outer planet ( $R_p \sim 100$  au) driving the tightly wound spirals in the outer regions could explain the observations. A similar two-planet configuration was proposed by Baruteau et al. (2019), who invoked a Jupiter-mass planet at 35 au, and a companion five times more massive at 140 au to simultaneously explain the scattered-light spirals and the two compact crescents in the millimeter continuum.

Another scenario consistent with the observed vertical spiral motions involves an eccentric circumstellar disc induced by a substellar companion in the innermost regions of the system. Ragusa et al. (2024) showed that a companion with a mass of about 10% that of the central star can excite moderate eccentricities in the outer disc ( $e \lesssim 0.2$ ), which in turn generate  $m = 1$  blueshifted and redshifted spiral patterns in the vertical velocity component, closely resembling the spiral structures observed in MWC 758. This interpretation is further supported by the measurable eccentricity of the dust cavity in this source ( $e \sim 0.1$  Dong et al. 2018), as well as by the comparable amplitudes of the vertical motions predicted in eccentric-disc models ( $\sim 0.4 \text{ km s}^{-1}$ ) and those inferred from our velocity spirals ( $\sim 0.3 \text{ km s}^{-1}$ ). Such large vertical velocities are difficult to reproduce via the planet-buoyancy spirals in the outer disc without invoking a very massive planet (Bae et al. 2021), making the eccentric-disc scenario one of the most compelling explanations for the observed features. We refer the reader to Benisty et al. (2026) for a broader discussion of vertical motions across the exoALMA sample.

An alternative explanation that does not necessarily require embedded companions was recently proposed by Winter et al. (2025), who demonstrated that the observed  $m = 1$  spiral structures in MWC 758 and other exoALMA targets can arise from moderately warped disc geometries. In these models, small radial variations of only a few degrees in inclination and position angle relative to the mean disc orientation can produce azimuthal asymmetries in the projected Keplerian ro-

tation that closely mimic the spiral kinematic patterns observed in this system.

## 6. CONCLUSIONS

In this work, we present a tomographic analysis of molecular-line properties designed to extract and characterize gas substructures in protoplanetary discs observed with ALMA. We first apply this methodology to synthetic observations of planet-disc interaction and disc-instability simulations to evaluate the detectability of localized substructures and line-profile perturbations driven by these mechanisms. We then apply the same framework on exoALMA CO observations of the discs around HD 135344B and MWC 758, where a variety of dust substructures have long been associated with planet-disc interactions. Our main findings are summarized as follows:

1. Through synthetic observations of planet-disc interaction simulations, we identify a correlation between the location of embedded planets and localized line broadening in the disc (Fig. 3). Using line-width enhancements as tracers of planets offers significant advantages over kinematic analyses based solely on line-centroid perturbations, as this observable is largely insensitive to the planet's azimuthal location and provides a higher degree of spatial clustering (Figs. 4, 6, and 7).
2. Planets with masses greater than 0.2% of the stellar mass (e.g.  $2 M_{\text{Jup}}$  for a  $1 M_\odot$  star) can be robustly detected through line-broadening signatures in discs of moderate inclination ( $i < 45^\circ$ ) under fiducial exoALMA observational setups. Importantly, achieving a high signal-to-noise ratio (SNR) at the planet's location is more critical for detection than high angular or spectral resolution (Figs. 5, 6, and 7). Increasing the SNR by a factor of  $\sim 8$  (e.g. by degrading the beam size from  $0''.15$  to  $0''.3$ ) enables the detection of planets with masses as low as 0.1% of the stellar mass, which would otherwise remain undetected even in discs at low inclinations ( $i < 30^\circ$ ).
3. Although disc instabilities can also produce localized velocity and line-width perturbations (Fig. 8), they can be distinguished from planet-driven signals by examining the morphology of the corresponding line profiles. Broadened optically thick lines in the vicinity of an embedded planet are asymmetric around the line centroid and exhibit an intensity deficit toward blueshifted velocities, consistent with partially resolved meridional flows

preferentially traced from the upper disc surface. In contrast, line broadening associated with disc instabilities is comparatively more isotropic, with intensity distributions concentrated closer to the line centroid (Figs. 9 and 10).

4. We identify evidence for the presence of unseen planets in the disc of HD 135344B. Based on the analysis of peak and clustered perturbations in velocity and line-width residuals, we propose three candidate locations for these companions. The first corresponds to a planet at  $R = 73$  au and  $\phi = 15^\circ$ , responsible for the observed line broadening across multiple vertical layers of the disc and exhibiting line asymmetries consistent with our planet-disc synthetic observations. The second is a more interior planet at  $R = 41$  au and  $\phi = 36^\circ$ , triggering increased velocity dispersions in the disc's upper layers (Fig. 12). The third candidate lies exterior to the continuum substructures and induces a Doppler-flip signature centered at  $R = 95$  au and  $\phi = -133^\circ$ , accompanied by a spiral-like line-width perturbation and large-scale velocity structures qualitatively reproduced by a PPDONET hydrodynamical model (Fig. 13). While these companions have been previously invoked to explain the substructures observed in the dust continuum emission, this work provides the first gas-based evidence supporting their presence (see Fig. 15 for a summary).
5. The disc of MWC 758 is dominated by large-scale perturbations in the form of spiral structures across all line diagnostics. The velocity spirals are tightly wound in the outer disc and spatially coincide with regions of enhanced line broadening, indicative of unresolved velocity flows or increased optical depths (Fig. 16). The most prominent spiral exhibits velocity amplitudes of  $\sim 0.2 - 0.3 \text{ km s}^{-1}$ , predominantly shaped by downward vertical motions, with a weaker interior blueshifted counterpart consistent with upward flows. Although a massive planet located exterior to the dust continuum substructures could, in principle, generate a similar velocity spiral, we do not identify any significantly localized perturbation that could be attributed to such a companion. Instead, scenarios involving a warped outer disc or a substellar object in the inner regions provide a more natural explanation for both the observed spiral velocities and the absence of localized signatures (see Fig. 17 for a summary).

## ACKNOWLEDGMENTS

We thank the anonymous referee for the constructive comments and suggestions, which greatly improved the quality of this work. This Letter makes use of the following ALMA data: ADS/JAO.ALMA#2021.1.01123.L. ALMA is a partnership of ESO (representing its member states), NSF (USA) and NINS (Japan), together with NRC (Canada), MOST and ASIAA (Taiwan), and KASI (Republic of Korea), in cooperation with the Republic of Chile. The Joint ALMA Observatory is operated by ESO, AUI/NRAO and NAOJ. The National Radio Astronomy Observatory is a facility of the National Science Foundation operated under cooperative agreement by Associated Universities, Inc. We thank the North American ALMA Science Center (NAASC) for their generous support including providing computing facilities and financial support for student attendance at workshops and publications. Support for AFI was provided by NASA through the NASA Hubble Fellowship grant No. HST-HF2-51532.001-A awarded by the Space Telescope Science Institute, which is operated by the Association of Universities for Research in Astronomy, Inc., for NASA, under contract NAS5-26555. JB acknowledges support from NASA XRP grant No. 80NSSC23K1312. SF is funded by the European Union (ERC, UNVEIL, 101076613), and acknowledges financial contribution from PRIN-MUR 2022YP5ACE. EFvD acknowledges support from the ERC grant 101019751 MOLDISK. MB, JS, DF have received funding from the European Research Council (ERC) under the European Union's Horizon 2020 research and innovation programme (PROTOPLANETS, grant agreement No. 101002188). PC and LT acknowledge support by the Italian Ministero dell'Istruzione, Università e Ricerca through the grant Progetti Premiali 2012 - iALMA (CUP C52I13000140001) and by the ANID BASAL project FB210003. NC has received funding from the European Research Council (ERC) under the European Union Horizon Europe research and innovation program (grant agreement No. 101042275, project StellarMADE). M. Flock has received funding from the European Research Council (ERC) under the European Unions Horizon 2020 research and innovation program (grant agreement No. 757957). M. Fukagawa is supported by a Grant-in-Aid from the Japan Society for the Promotion of Science (KAKENHI: No. JP22H01274). CH acknowledges support from NSF AAG grant No. 2407679. JDI acknowledges support from an STFC Ernest Rutherford Fellowship (ST/W004119/1) and a University Academic Fellowship from the University of Leeds. AI acknowledges support from the National Aeronautics and Space Administration under grant

No. 80NSSC18K0828. G. Lodato has received funding from the European Union’s Horizon 2020 research and innovation program under the Marie Skłodowska-Curie grant agreement No. 823823 (DUSTBUSTERS), from PRIN-MUR 20228JPA3A and the European Union Next Generation EU, CUP: G53D23000870006. CL has received funding from the European Union’s Horizon 2020 research and innovation program under the Marie Skłodowska-Curie grant agreement No. 823823 (DUSTBUSTERS) and by the UK Science and Technology research Council (STFC) via the consolidated grant ST/W000997/1. FMe has received funding from the European Research Council (ERC) under the European Union’s Horizon Europe research and innovation program (grant agreement No. 101053020, project Dust2Planets). CP acknowledges Australian Research Council funding via FT170100040, DP18010423, DP220103767, and DP240103290. DP acknowledges Australian Research Council funding via DP18010423, DP220103767, and DP240103290. GR acknowledges funding from the Fondazione Cariplo, grant no. 2022-1217, and the European Research Council (ERC) under the European Union’s Horizon Europe Research & Innovation Programme under grant agreement no. 101039651 (DiscEvol). AJW has received funding from

the European Union’s Horizon 2020 research and innovation programme under the Marie Skłodowska-Curie grant agreement No 101104656. Support for BZ was provided by The Brinson Foundation. This work was partly supported by the Deutsche Forschungsgemeinschaft (DFG, German Research Foundation) - Ref no. 325594231 FOR 2634/2 TE 1024/2-1, and by the DFG Cluster of Excellence Origins ([www.origins-cluster.de](http://www.origins-cluster.de)). This project has received funding from the European Research Council (ERC) via the ERC Synergy Grant ECOGAL (grant 855130). Views and opinions expressed by ERC-funded scientists are however those of the author(s) only and do not necessarily reflect those of the European Union or the European Research Council. Neither the European Union nor the granting authority can be held responsible for them.

*Software:* ASTROPY ([Astropy Collaboration et al. 2022](#)), BETTERMOMENTS ([Teague & Foreman-Mackey 2018](#)), CASA ([CASA Team et al. 2022](#)), CMASHER ([van der Velden 2020](#)), DISCMINER ([Izquierdo et al. 2021](#)), EMCEE ([Foreman-Mackey et al. 2013](#)), MATPLOTLIB ([Hunter 2007](#)), NUMPY ([Harris et al. 2020](#)), SCIKIT-IMAGE ([van der Walt et al. 2014](#)), SCIPY ([Virtanen et al. 2020](#)), RADIO-BEAM ([Koch et al. 2021](#)), SPECTRAL-CUBE ([Ginsburg et al. 2019](#))

## REFERENCES

- Andrews, S. M., Huang, J., Pérez, L. M., et al. 2018, *ApJL*, 869, L41, doi: [10.3847/2041-8213/aaf741](https://doi.org/10.3847/2041-8213/aaf741)
- Astropy Collaboration, Price-Whelan, A. M., Lim, P. L., et al. 2022, *ApJ*, 935, 167, doi: [10.3847/1538-4357/ac7c74](https://doi.org/10.3847/1538-4357/ac7c74)
- Bae, J., Isella, A., Zhu, Z., et al. 2023, in *Astronomical Society of the Pacific Conference Series*, Vol. 534, *Astronomical Society of the Pacific Conference Series*, ed. S. Inutsuka, Y. Aikawa, T. Muto, K. Tomida, & M. Tamura, 423
- Bae, J., Teague, R., & Zhu, Z. 2021, *ApJ*, 912, 56, doi: [10.3847/1538-4357/abe45e](https://doi.org/10.3847/1538-4357/abe45e)
- Bae, J., Zhu, Z., & Hartmann, L. 2016, *ApJ*, 819, 134, doi: [10.3847/0004-637X/819/2/134](https://doi.org/10.3847/0004-637X/819/2/134)
- Bae, J., Teague, R., Andrews, S. M., et al. 2022, *ApJL*, 934, L20, doi: [10.3847/2041-8213/ac7fa3](https://doi.org/10.3847/2041-8213/ac7fa3)
- Bae, J., Flock, M., Izquierdo, A., et al. 2025, *ApJL*, 984, L12, doi: [10.3847/2041-8213/adc436](https://doi.org/10.3847/2041-8213/adc436)
- Barraza-Alfaro, M., Flock, M., Marino, S., & Pérez, S. 2021, *A&A*, 653, A113, doi: [10.1051/0004-6361/202140535](https://doi.org/10.1051/0004-6361/202140535)
- Barraza-Alfaro, M., Flock, M., Béthune, W., et al. 2025, *ApJL*, 984, L21, doi: [10.3847/2041-8213/adc42d](https://doi.org/10.3847/2041-8213/adc42d)
- Baruteau, C., Barraza, M., Pérez, S., et al. 2019, *MNRAS*, 486, 304, doi: [10.1093/mnras/stz802](https://doi.org/10.1093/mnras/stz802)
- Benisty, M., Izquierdo, A., & Stadler, J. 2026, *ApJL*, TBD
- Benisty, M., Juhasz, A., Boccaletti, A., et al. 2015, *A&A*, 578, L6, doi: [10.1051/0004-6361/201526011](https://doi.org/10.1051/0004-6361/201526011)
- Benítez-Llambay, P., & Masset, F. S. 2016, *ApJS*, 223, 11, doi: [10.3847/0067-0049/223/1/11](https://doi.org/10.3847/0067-0049/223/1/11)
- Béthune, W., & Latter, H. 2022, *A&A*, 663, A138, doi: [10.1051/0004-6361/202243219](https://doi.org/10.1051/0004-6361/202243219)
- Blum, H. 1967, in *Models for the Perception of Speech and Visual Form*, ed. W. Wathen-Dunn (Cambridge: MIT Press), 362–380
- Boehler, Y., Ricci, L., Weaver, E., et al. 2018, *ApJ*, 853, 162, doi: [10.3847/1538-4357/aaa19c](https://doi.org/10.3847/1538-4357/aaa19c)
- Calcino, J., Christiaens, V., Price, D. J., et al. 2020, *MNRAS*, 498, 639, doi: [10.1093/mnras/staa2468](https://doi.org/10.1093/mnras/staa2468)
- Calcino, J., Hilder, T., Price, D. J., et al. 2022, *ApJL*, 929, L25, doi: [10.3847/2041-8213/ac64a7](https://doi.org/10.3847/2041-8213/ac64a7)
- CASA Team, Bean, B., Bhatnagar, S., et al. 2022, *PASP*, 134, 114501, doi: [10.1088/1538-3873/ac9642](https://doi.org/10.1088/1538-3873/ac9642)
- Casassus, S., & Pérez, S. 2019, *ApJL*, 883, L41, doi: [10.3847/2041-8213/ab4425](https://doi.org/10.3847/2041-8213/ab4425)
- Casassus, S., Christiaens, V., Cárcamo, M., et al. 2021, *MNRAS*, 507, 3789, doi: [10.1093/mnras/stab2359](https://doi.org/10.1093/mnras/stab2359)

- Cazzoletti, P., van Dishoeck, E. F., Pinilla, P., et al. 2018, *A&A*, 619, A161, doi: [10.1051/0004-6361/201834006](https://doi.org/10.1051/0004-6361/201834006)
- Cugno, G., Leisenring, J., Wagner, K. R., et al. 2024, *AJ*, 167, 182, doi: [10.3847/1538-3881/ad1ffc](https://doi.org/10.3847/1538-3881/ad1ffc)
- Curone, P., Facchini, S., Andrews, S. M., et al. 2025, *ApJL*, 984, L9, doi: [10.3847/2041-8213/adc438](https://doi.org/10.3847/2041-8213/adc438)
- Dartois, E., Dutrey, A., & Guilloteau, S. 2003, *A&A*, 399, 773, doi: [10.1051/0004-6361:20021638](https://doi.org/10.1051/0004-6361:20021638)
- Dong, R., Liu, S.-Y., & Fung, J. 2019, *ApJ*, 870, 72, doi: [10.3847/1538-4357/aaf38e](https://doi.org/10.3847/1538-4357/aaf38e)
- Dong, R., Zhu, Z., Rafikov, R. R., & Stone, J. M. 2015, *ApJL*, 809, L5, doi: [10.1088/2041-8205/809/1/L5](https://doi.org/10.1088/2041-8205/809/1/L5)
- Dong, R., Liu, S.-y., Eisner, J., et al. 2018, *ApJ*, 860, 124, doi: [10.3847/1538-4357/aac6cb](https://doi.org/10.3847/1538-4357/aac6cb)
- Dullemond, C. P., Juhasz, A., Pohl, A., et al. 2012, RADMC-3D: A multi-purpose radiative transfer tool, *Astrophysics Source Code Library*, record ascl:1202.015. <http://ascl.net/1202.015>
- Fairlamb, J. R., Oudmaijer, R. D., Mendigutía, I., Ilee, J. D., & van den Ancker, M. E. 2015, *MNRAS*, 453, 976, doi: [10.1093/mnras/stv1576](https://doi.org/10.1093/mnras/stv1576)
- Flock, M., Ruge, J. P., Dzyurkevich, N., et al. 2015, *A&A*, 574, A68, doi: [10.1051/0004-6361/201424693](https://doi.org/10.1051/0004-6361/201424693)
- Flock, M., Turner, N. J., Nelson, R. P., et al. 2020, *ApJ*, 897, 155, doi: [10.3847/1538-4357/ab9641](https://doi.org/10.3847/1538-4357/ab9641)
- Foreman-Mackey, D., Hogg, D. W., Lang, D., & Goodman, J. 2013, *PASP*, 125, 306, doi: [10.1086/670067](https://doi.org/10.1086/670067)
- Fukagawa, M., Izquierdo, A., & Facchini, S. 2026, *ApJL*, TBD
- Gaia Collaboration, Vallenari, A., Brown, A. G. A., et al. 2023, *A&A*, 674, A1, doi: [10.1051/0004-6361/202243940](https://doi.org/10.1051/0004-6361/202243940)
- Galloway-Sprietsma, M., Bae, J., Izquierdo, A. F., et al. 2025, *ApJL*, 984, L10, doi: [10.3847/2041-8213/adc437](https://doi.org/10.3847/2041-8213/adc437)
- Garufi, A., Quanz, S. P., Avenhaus, H., et al. 2013, *A&A*, 560, A105, doi: [10.1051/0004-6361/201322429](https://doi.org/10.1051/0004-6361/201322429)
- Ginsburg, A., Koch, E., Robitaille, T., et al. 2019, radio-astro-tools/spectral-cube: Release v0.4.5, v0.4.5, Zenodo, doi: [10.5281/zenodo.3558614](https://doi.org/10.5281/zenodo.3558614)
- Grady, C. A., Muto, T., Hashimoto, J., et al. 2013, *ApJ*, 762, 48, doi: [10.1088/0004-637X/762/1/48](https://doi.org/10.1088/0004-637X/762/1/48)
- Hacar, A., Alves, J., Burkert, A., & Goldsmith, P. 2016, *A&A*, 591, A104, doi: [10.1051/0004-6361/201527319](https://doi.org/10.1051/0004-6361/201527319)
- Hall, C., Dong, R., Teague, R., et al. 2020, *ApJ*, 904, 148, doi: [10.3847/1538-4357/abac17](https://doi.org/10.3847/1538-4357/abac17)
- Harris, C. R., Millman, K. J., van der Walt, S. J., et al. 2020, *Nature*, 585, 357, doi: [10.1038/s41586-020-2649-2](https://doi.org/10.1038/s41586-020-2649-2)
- Hunter, J. D. 2007, *Computing in Science Engineering*, 9, 90, doi: [10.1109/MCSE.2007.55](https://doi.org/10.1109/MCSE.2007.55)
- Izquierdo, A. F., Facchini, S., Rosotti, G. P., van Dishoeck, E. F., & Testi, L. 2022, *ApJ*, 928, 2, doi: [10.3847/1538-4357/ac474d](https://doi.org/10.3847/1538-4357/ac474d)
- Izquierdo, A. F., Testi, L., Facchini, S., Rosotti, G. P., & van Dishoeck, E. F. 2021, *A&A*, 650, A179, doi: [10.1051/0004-6361/202140779](https://doi.org/10.1051/0004-6361/202140779)
- Izquierdo, A. F., Testi, L., Facchini, S., et al. 2023, *A&A*, 674, A113, doi: [10.1051/0004-6361/202245425](https://doi.org/10.1051/0004-6361/202245425)
- Izquierdo, A. F., Stadler, J., Galloway-Sprietsma, M., et al. 2025, *ApJL*, 984, L8, doi: [10.3847/2041-8213/adc439](https://doi.org/10.3847/2041-8213/adc439)
- Izquierdo, A. F., Bae, J., Galloway-Sprietsma, M., et al. 2026, *ApJL*, 997, L2, doi: [10.3847/2041-8213/ae2f59](https://doi.org/10.3847/2041-8213/ae2f59)
- Koch, E., Ginsburg, A., AKL, et al. 2021, radio-astro-tools/radio-beam: v0.3.3, v0.3.3, Zenodo, doi: [10.5281/zenodo.4623788](https://doi.org/10.5281/zenodo.4623788)
- Koch, E. W., & Rosolowsky, E. W. 2015, *MNRAS*, 452, 3435, doi: [10.1093/mnras/stv1521](https://doi.org/10.1093/mnras/stv1521)
- Law, C. J., Booth, A. S., & Öberg, K. I. 2023, *ApJL*, 952, L19, doi: [10.3847/2041-8213/acdfd0](https://doi.org/10.3847/2041-8213/acdfd0)
- Lesur, G., Flock, M., Ercolano, B., et al. 2023, in *Astronomical Society of the Pacific Conference Series*, Vol. 534, *Astronomical Society of the Pacific Conference Series*, ed. S. Inutsuka, Y. Aikawa, T. Muto, K. Tomida, & M. Tamura, 465
- Leys, C., Ley, C., Klein, O., Bernard, P., & Licata, L. 2013, *Journal of Experimental Social Psychology*, 49, 764, doi: <https://doi.org/10.1016/j.jesp.2013.03.013>
- Longarini, C., Lodato, G., Rosotti, G., et al. 2025, *ApJL*, 984, L17, doi: [10.3847/2041-8213/adc431](https://doi.org/10.3847/2041-8213/adc431)
- Loomis, R. A., Facchini, S., Benisty, M., et al. 2025, *ApJL*, 984, L7, doi: [10.3847/2041-8213/adc43a](https://doi.org/10.3847/2041-8213/adc43a)
- Maior, F., Fedele, D., Roccatagliata, V., et al. 2025, *A&A*, 699, L10, doi: [10.1051/0004-6361/202554472](https://doi.org/10.1051/0004-6361/202554472)
- Mao, S., Dong, R., Lu, L., et al. 2023, *ApJL*, 950, L12, doi: [10.3847/2041-8213/acd77f](https://doi.org/10.3847/2041-8213/acd77f)
- Mignone, A., Bodo, G., Massaglia, S., et al. 2007, *ApJS*, 170, 228, doi: [10.1086/513316](https://doi.org/10.1086/513316)
- Miotello, A., Kamp, I., Birnstiel, T., Cleaves, L. C., & Kataoka, A. 2023, in *Astronomical Society of the Pacific Conference Series*, Vol. 534, *Astronomical Society of the Pacific Conference Series*, ed. S. Inutsuka, Y. Aikawa, T. Muto, K. Tomida, & M. Tamura, 501, doi: [10.48550/arXiv.2203.09818](https://doi.org/10.48550/arXiv.2203.09818)
- Muto, T., Grady, C. A., Hashimoto, J., et al. 2012, *ApJL*, 748, L22, doi: [10.1088/2041-8205/748/2/L22](https://doi.org/10.1088/2041-8205/748/2/L22)
- Öberg, K. I., Facchini, S., & Anderson, D. E. 2023, *ARA&A*, 61, 287, doi: [10.1146/annurev-astro-022823-040820](https://doi.org/10.1146/annurev-astro-022823-040820)
- Öberg, K. I., Guzmán, V. V., Walsh, C., et al. 2021, *ApJS*, 257, 1, doi: [10.3847/1538-4365/ac1432](https://doi.org/10.3847/1538-4365/ac1432)

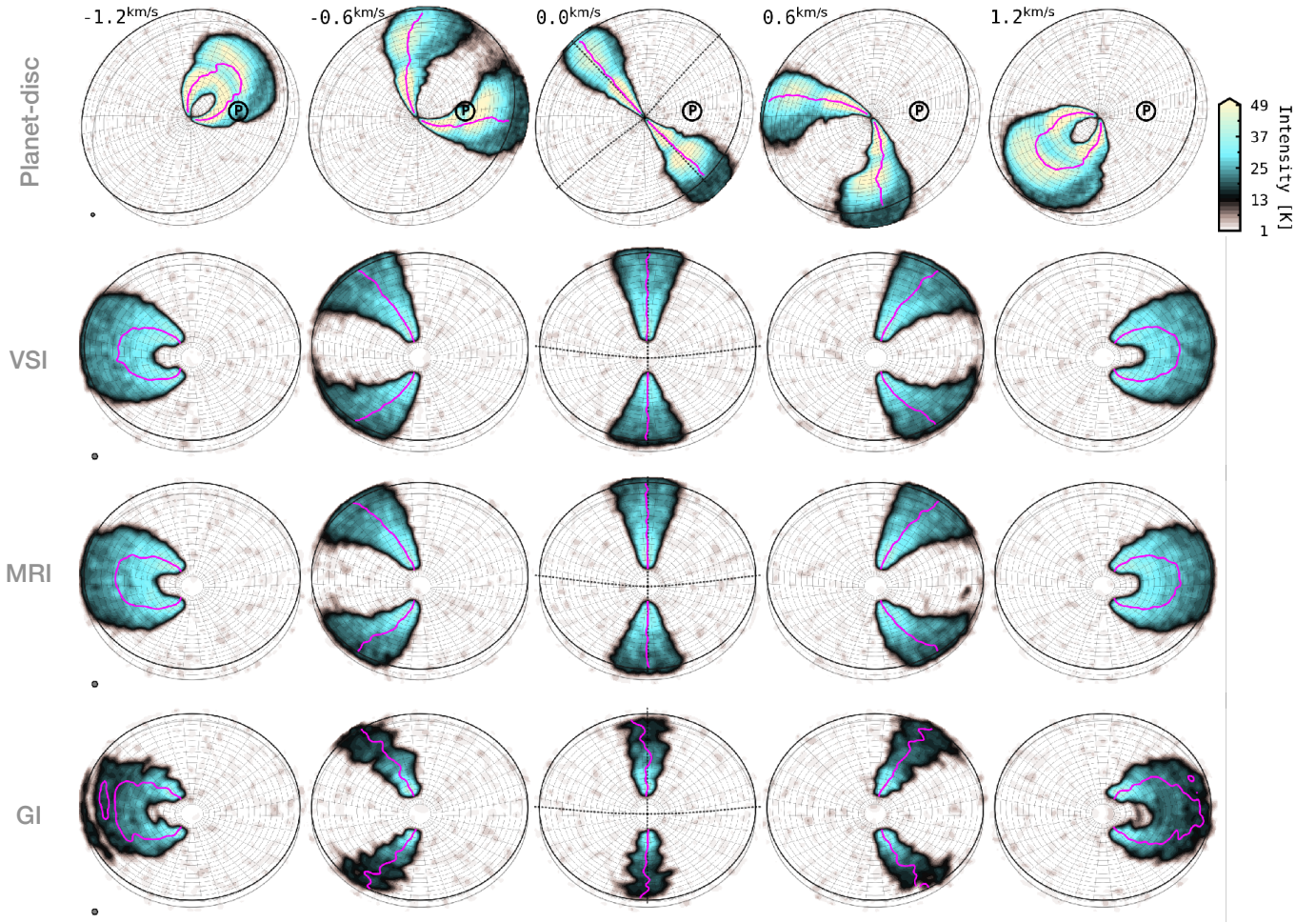
- Pérez, S., Casassus, S., & Benítez-Llambay, P. 2018, *MNRAS*, 480, L12, doi: [10.1093/mnras/sly109](https://doi.org/10.1093/mnras/sly109)
- Pinte, C., Teague, R., Flaherty, K., et al. 2023, in *Astronomical Society of the Pacific Conference Series*, Vol. 534, *Astronomical Society of the Pacific Conference Series*, ed. S. Inutsuka, Y. Aikawa, T. Muto, K. Tomida, & M. Tamura, 645
- Pinte, C., Price, D. J., Ménard, F., et al. 2018, *ApJL*, 860, L13, doi: [10.3847/2041-8213/aac6dc](https://doi.org/10.3847/2041-8213/aac6dc)
- Pinte, C., van der Plas, G., Ménard, F., et al. 2019, *Nature Astronomy*, 3, 1109, doi: [10.1038/s41550-019-0852-6](https://doi.org/10.1038/s41550-019-0852-6)
- Pinte, C., Ilee, J. D., Huang, J., et al. 2025, *ApJL*, 984, L15, doi: [10.3847/2041-8213/adc433](https://doi.org/10.3847/2041-8213/adc433)
- Rabago, I., & Zhu, Z. 2021, *MNRAS*, 502, 5325, doi: [10.1093/mnras/stab447](https://doi.org/10.1093/mnras/stab447)
- Ragusa, E., Lynch, E., Laibe, G., Longarini, C., & Ceppi, S. 2024, *A&A*, 686, A264, doi: [10.1051/0004-6361/202449583](https://doi.org/10.1051/0004-6361/202449583)
- Reggiani, M., Christiaens, V., Absil, O., et al. 2018, *A&A*, 611, A74, doi: [10.1051/0004-6361/201732016](https://doi.org/10.1051/0004-6361/201732016)
- Ren, B., Dong, R., van Holstein, R. G., et al. 2020, *ApJL*, 898, L38, doi: [10.3847/2041-8213/aba43e](https://doi.org/10.3847/2041-8213/aba43e)
- Ren, B. B., Benisty, M., Ginski, C., et al. 2023, *A&A*, 680, A114, doi: [10.1051/0004-6361/202347353](https://doi.org/10.1051/0004-6361/202347353)
- Rosotti, G. P., Teague, R., Dullemond, C., Booth, R. A., & Clarke, C. J. 2020, *MNRAS*, 495, 173, doi: [10.1093/mnras/staa1170](https://doi.org/10.1093/mnras/staa1170)
- Schwarz, K. R., Bergin, E. A., Cleves, L. I., et al. 2016, *ApJ*, 823, 91, doi: [10.3847/0004-637X/823/2/91](https://doi.org/10.3847/0004-637X/823/2/91)
- Speedie, J., Dong, R., Hall, C., et al. 2024, *Nature*, 633, 58, doi: [10.1038/s41586-024-07877-0](https://doi.org/10.1038/s41586-024-07877-0)
- Stadler, J., Benisty, M., Izquierdo, A., et al. 2023, *A&A*, 670, L1, doi: [10.1051/0004-6361/202245381](https://doi.org/10.1051/0004-6361/202245381)
- Stadler, J., Benisty, M., Winter, A. J., et al. 2025, *ApJL*, 984, L11, doi: [10.3847/2041-8213/adb152](https://doi.org/10.3847/2041-8213/adb152)
- Stolker, T., Dominik, C., Avenhaus, H., et al. 2016, *A&A*, 595, A113, doi: [10.1051/0004-6361/201528039](https://doi.org/10.1051/0004-6361/201528039)
- Teague, R., Bae, J., & Bergin, E. A. 2019, *Nature*, 574, 378, doi: [10.1038/s41586-019-1642-0](https://doi.org/10.1038/s41586-019-1642-0)
- Teague, R., Bae, J., Bergin, E. A., Birnstiel, T., & Foreman-Mackey, D. 2018, *ApJL*, 860, L12, doi: [10.3847/2041-8213/aac6d7](https://doi.org/10.3847/2041-8213/aac6d7)
- Teague, R., & Foreman-Mackey, D. 2018, *Research Notes of the American Astronomical Society*, 2, 173, doi: [10.3847/2515-5172/aae265](https://doi.org/10.3847/2515-5172/aae265)
- Teague, R., Bae, J., Aikawa, Y., et al. 2021, *ApJS*, 257, 18, doi: [10.3847/1538-4365/ac1438](https://doi.org/10.3847/1538-4365/ac1438)
- Teague, R., Benisty, M., Facchini, S., et al. 2025, *ApJL*, 984, L6, doi: [10.3847/2041-8213/adc43b](https://doi.org/10.3847/2041-8213/adc43b)
- van der Marel, N., Cazzoletti, P., Pinilla, P., & Garufi, A. 2016, *ApJ*, 832, 178, doi: [10.3847/0004-637X/832/2/178](https://doi.org/10.3847/0004-637X/832/2/178)
- van der Velden, E. 2020, *The Journal of Open Source Software*, 5, 2004, doi: [10.21105/joss.02004](https://doi.org/10.21105/joss.02004)
- van der Walt, S., Schönberger, J. L., Nunez-Iglesias, J., et al. 2014, *PeerJ*, 2, e453, doi: [10.7717/peerj.453](https://doi.org/10.7717/peerj.453)
- Virtanen, P., Gommers, R., Burovski, E., et al. 2020, *scipy/scipy: SciPy 1.5.3, v1.5.3*, Zenodo, doi: [10.5281/zenodo.4100507](https://doi.org/10.5281/zenodo.4100507)
- Visser, R., van Dishoeck, E. F., & Black, J. H. 2009, *A&A*, 503, 323, doi: [10.1051/0004-6361/200912129](https://doi.org/10.1051/0004-6361/200912129)
- Wagner, K., Stone, J., Skemer, A., et al. 2023, *Nature Astronomy*, doi: [10.1038/s41550-023-02028-3](https://doi.org/10.1038/s41550-023-02028-3)
- Winter, A. J., Benisty, M., Izquierdo, A. F., et al. 2025, *ApJL*, 990, L10, doi: [10.3847/2041-8213/adf113](https://doi.org/10.3847/2041-8213/adf113)
- Wölfer, L., Facchini, S., van der Marel, N., et al. 2023, *A&A*, 670, A154, doi: [10.1051/0004-6361/202243601](https://doi.org/10.1051/0004-6361/202243601)
- Wölfer, L., Barraza-Alfaro, M., Teague, R., et al. 2025, *ApJL*, 984, L22, doi: [10.3847/2041-8213/adc42c](https://doi.org/10.3847/2041-8213/adc42c)
- Xie, C., Xie, C., Ren, B. B., et al. 2024, *Universe*, 10, 465, doi: [10.3390/universe10120465](https://doi.org/10.3390/universe10120465)

## APPENDIX

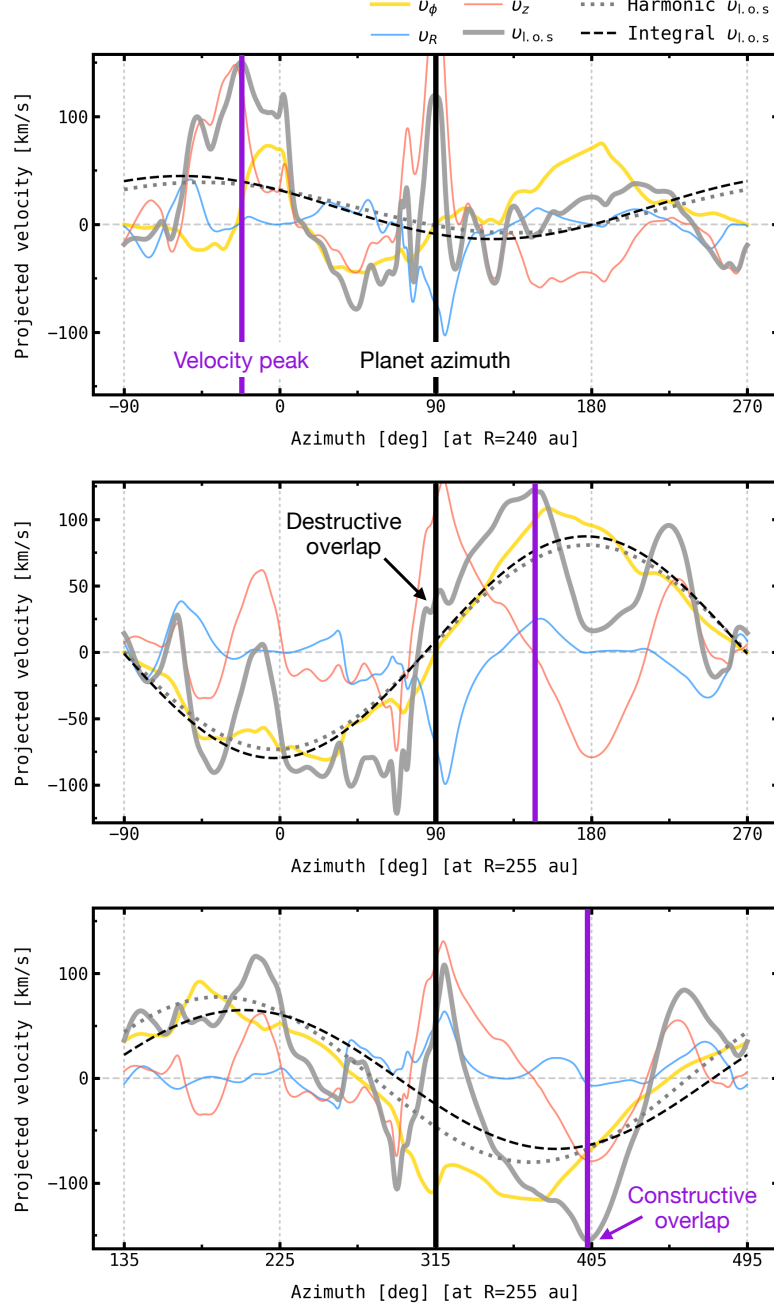
Here we provide complementary figures that support the results presented in the main text. Figure 18 illustrates selected  $^{12}\text{CO}$  channel maps from the synthetic observations of the planet-disc interaction and disc-instability simulations introduced in Sect. 3. Figure 19 presents azimuthal profiles of projected velocity components from planet-disc interaction simulations, demonstrating how the constructive or destructive overlap of velocities can induce strong signals in this observable away from the planet location. Figure 20 summarizes the key line diagnostics used to distinguish planet-driven signatures in velocity or line-width residual maps. Figure 21 presents the detection score (defined in Sect. 3.2.1) for planet-driven velocity peaks, complementing the scores based on line-width enhancements (Fig. 5).

Figure 22 illustrates edge-on slices of the vertical velocity component from planet-disc interaction simulations with planet masses of 0.1 and 0.2% of the stellar mass. This figure demonstrates that converging downward flows are localized to the planet's vicinity and are responsible for the line asymmetries discussed in Sect. 3.3. Figure 23 shows the absence of line asymmetries in optically thin emission, where planet-driven flows influence the line profile equally from both the front and back sides of the disc. This contrasts with the optically thick case, where a redshifted excess is induced in the lines around the planet due to the dominant front-side contribution (Fig. 9). Line broadening associated with localized features in the disc-instability simulations remains symmetric in both optically thin and thick emission.

Figure 24 shows the locations of peak velocity gradients in the azimuthal direction for the disc of HD 135344B, which help identify Doppler flips potentially associated with embedded planets (see Sect. 4.1.1). Finally, Figure 25 summarizes the extraction of large-scale kinematic structures in the disc of MWC 758, together with their pitch-angle and width profiles.



**Figure 18.** Selected  $^{12}\text{CO } J = 3 \rightarrow 2$  channel maps for the physical mechanisms studied in Sect. 3, shown for a disc inclination of  $i = -30^\circ$ . The channels in the top row correspond to synthetic observations of the planet-disc interaction model with a planet-to-star mass ratio of  $q = 2 \times 10^{-3}$  and a planet azimuth of  $\phi_p = -45^\circ$  in the disc reference frame; the projected planet location is labeled “P”. The beam size is shown by the filled circle in the lower left of the first-column panels. The magenta line denotes the isovelocity contour at the velocity of each channel, measured from the corresponding centroid velocity map.



**Figure 19.** Illustrating how the combined contributions of velocity components from a planet-disc interaction simulation ( $q = 2 \times 10^{-3}$ , before postprocessing), after subtraction of Keplerian motion, can naturally produce peak line-of-sight velocity residuals at azimuthal locations far from the embedded planet, either through constructive overlap of the projected velocities away from the planet or destructive addition near it. The violet and black vertical lines denote the azimuth of the projected peak velocity and the true planet azimuth, respectively. The top two panels show azimuthal profiles of the projected velocities at radii of 240 au (top) and 255 au (middle) for a planet located at an azimuth of  $\phi_p = 90^\circ$  and orbital radius  $R_p = 240$  au. The bottom row is analogous to the middle but for a planet at  $\phi_p = 315^\circ$ . All projected velocities were computed assuming a disc inclination of  $-30^\circ$  and an emission surface at  $z/r = 0.2$ . *Harmonic*  $v_{l.o.s}$  refers to the reconstructed velocity profile obtained by forward fitting the velocity components in the  $v_{l.o.s}$  equation (i.e. Eq. 3 of Izquierdo et al. 2025), assuming they are constant in azimuth, while *Integral*  $v_{l.o.s}$  follows the analytic solution introduced in Izquierdo et al. (2023).

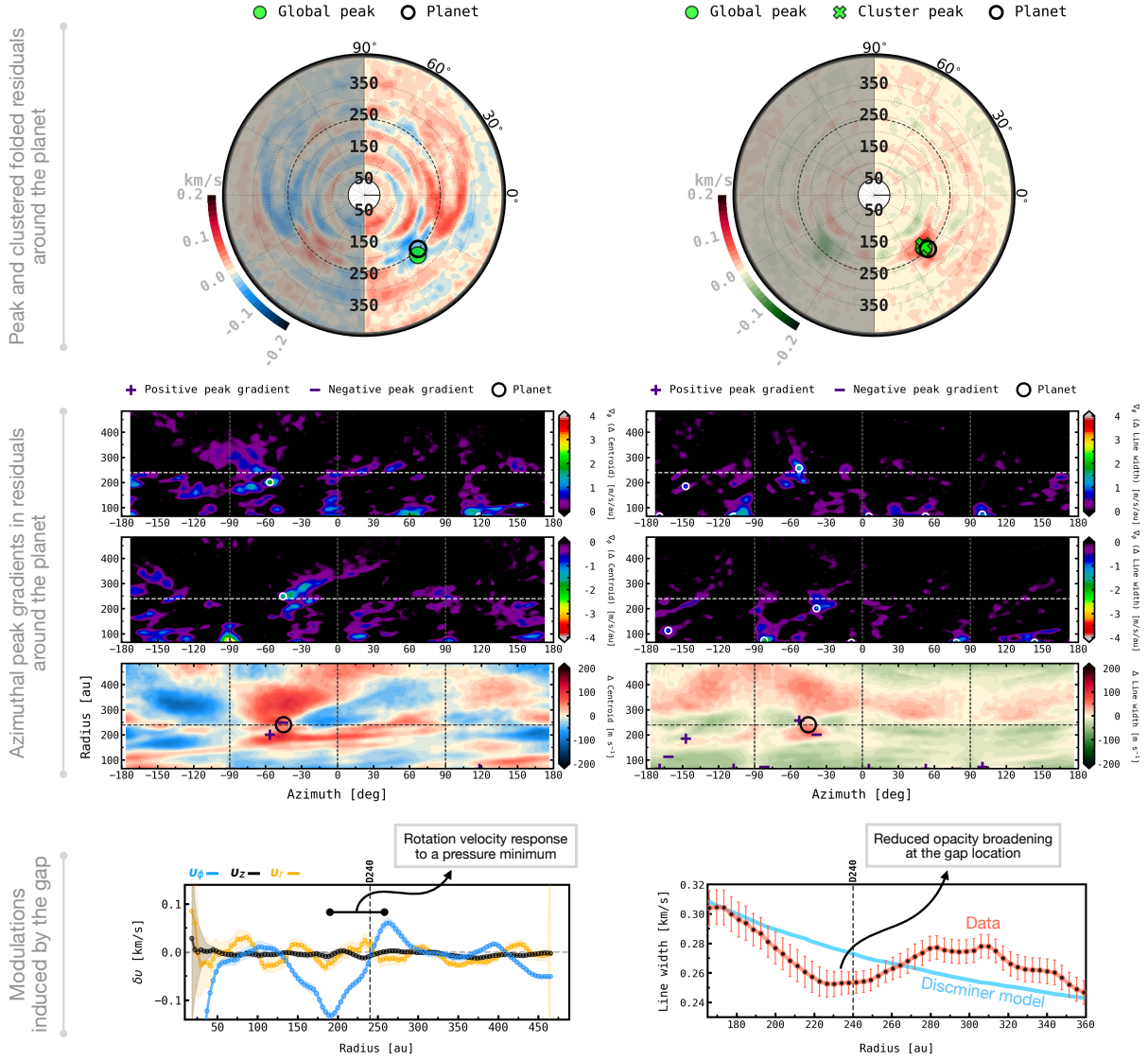


**Figure 20.** Summary of planet-driven signatures identified in the velocity and line-width residuals traced by  $^{12}\text{CO}$  emission from a planet-disc interaction simulation with a planet-to-star mass ratio of  $q \sim 2 \times 10^{-3}$ , assuming a disc inclination of  $i = -30^\circ$  and postprocessed with a fiducial beam size of  $0''.15$ . The planet is embedded at an orbital radius of 240 au and an azimuth of  $-45^\circ$ . See Section 3 for details of the simulation and postprocessing setups.

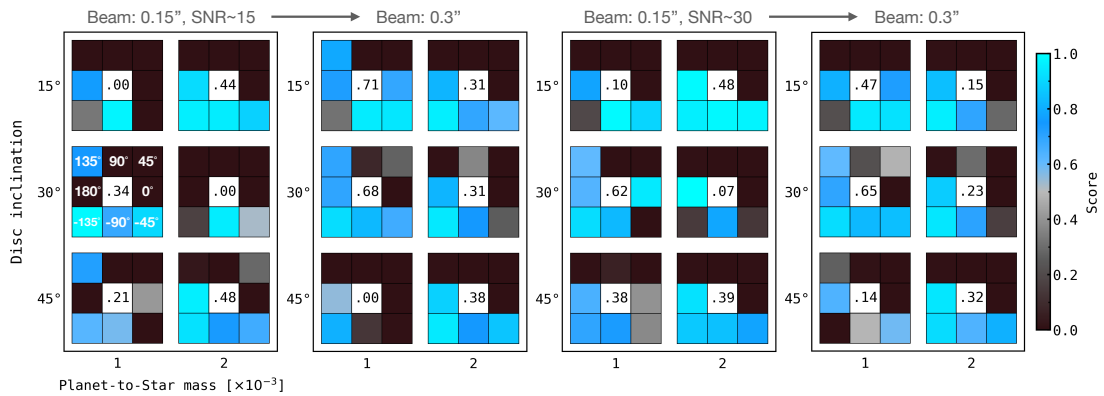


**Figure 21.** As Fig. 5 but for detections based on localized velocity residuals.

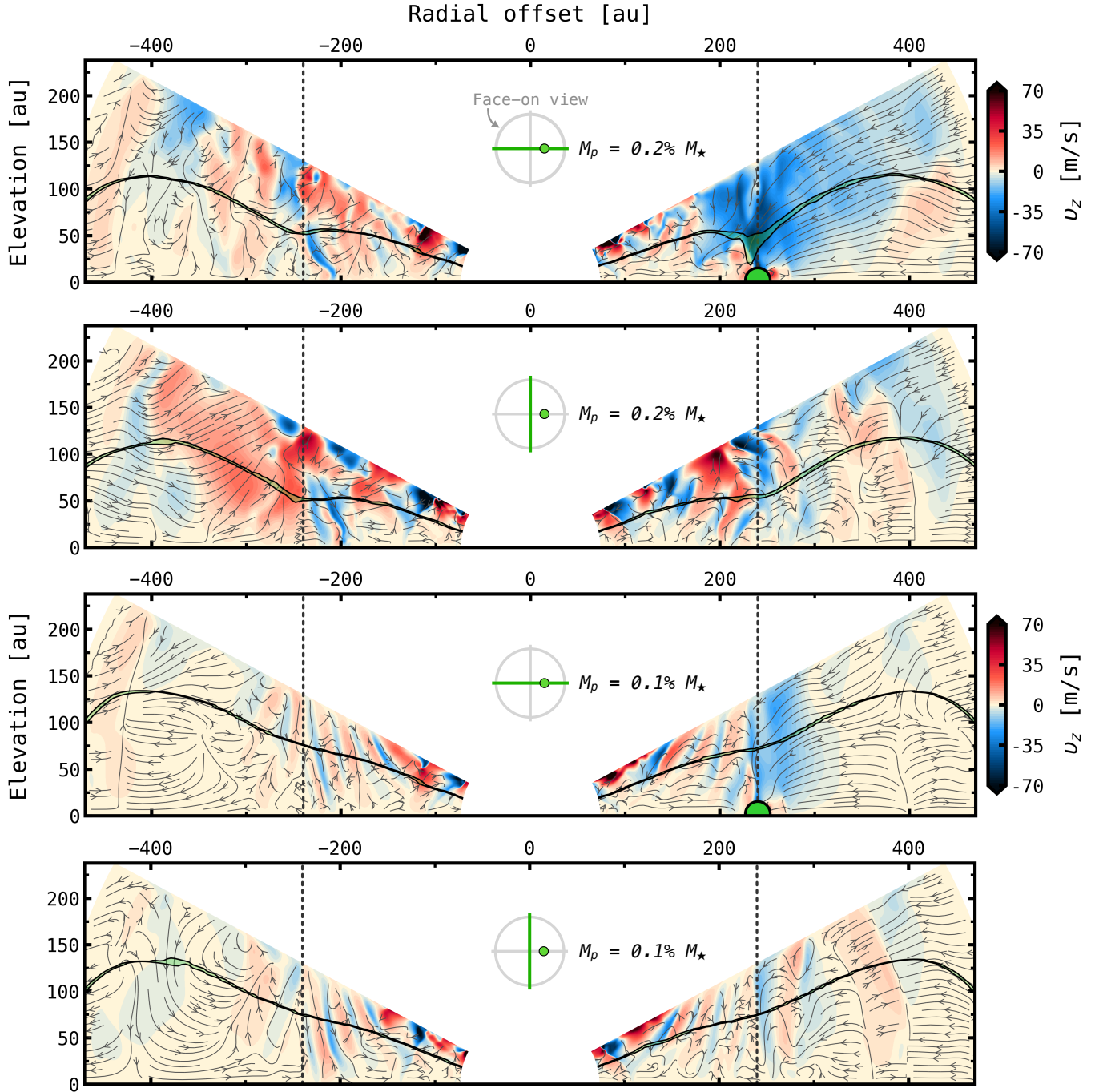


**Figure 22.** Edge-on slices of the vertical velocity component from the planet-disc interaction simulations presented in this work, overlaid with streamlines that incorporate the radial velocity field. The first and third panels from top to bottom show slices taken along the planet azimuth, while the second and fourth panels depict slices perpendicular to it. Optical depth  $\tau = 1$  surfaces representative of the  $^{12}\text{CO}$  emitting region are overlaid as solid black curves, with the region between the minimum and maximum  $\tau = 1$  elevations within a  $\pm 10^\circ$  wedge shaded in green. The strong localized downward flows around the planets are the primary drivers of the line-width enhancements and asymmetries identified in Sect. 3.

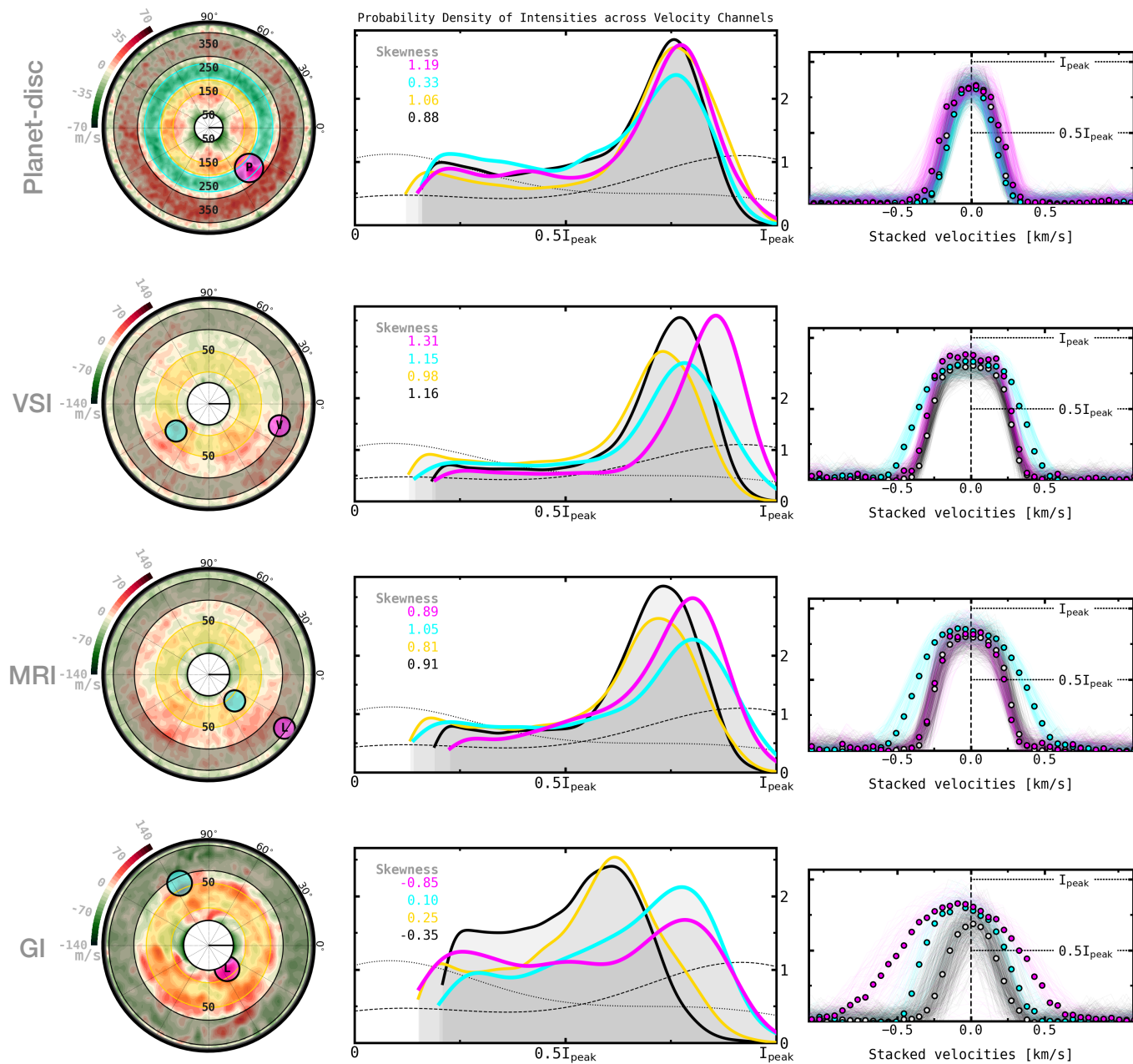


**Figure 23.** As Fig. 9 but for synthetic cubes of  $^{13}\text{CO } J = 3 \rightarrow 2$  line emission, assuming a  $^{12}\text{CO}/^{13}\text{CO}$  abundance ratio of 77.

## HD 135344B

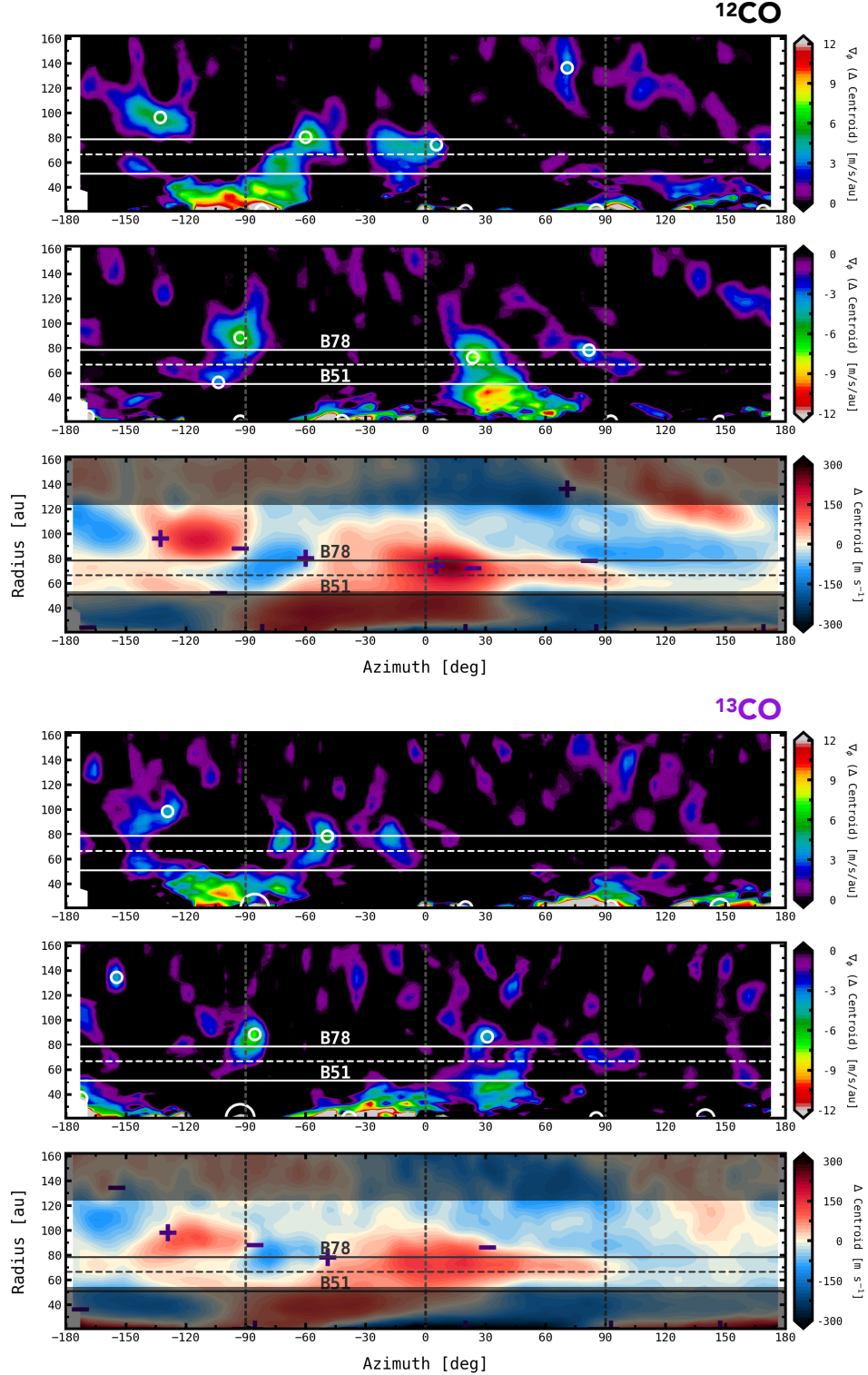


**Figure 24.** Polar maps illustrating the azimuthal gradients of the velocity residuals in the disc of HD 135344B, derived from  $^{12}\text{CO}$  and  $^{13}\text{CO}$  observations. The top and middle sub-panels show the positive and negative gradient components, respectively, while the bottom panels display the corresponding velocity residuals, enabling the identification of Doppler-flip signatures in the kinematics. White circles mark the locations of the steepest gradients exceeding a threshold of  $2.5 \text{ m s}^{-1} \text{ au}^{-1}$ , corresponding to velocity shifts greater than half the channel spacing per beam size (i.e.  $50 \text{ m s}^{-1} \text{ beam}^{-1}$ ). Pluses and minuses overlaid on the velocity residuals indicate the sign of the peak azimuthal gradients and highlight the central locations of the Doppler flips. Solid and dashed lines denote the radial separations of millimeter dust rings and gaps, respectively.

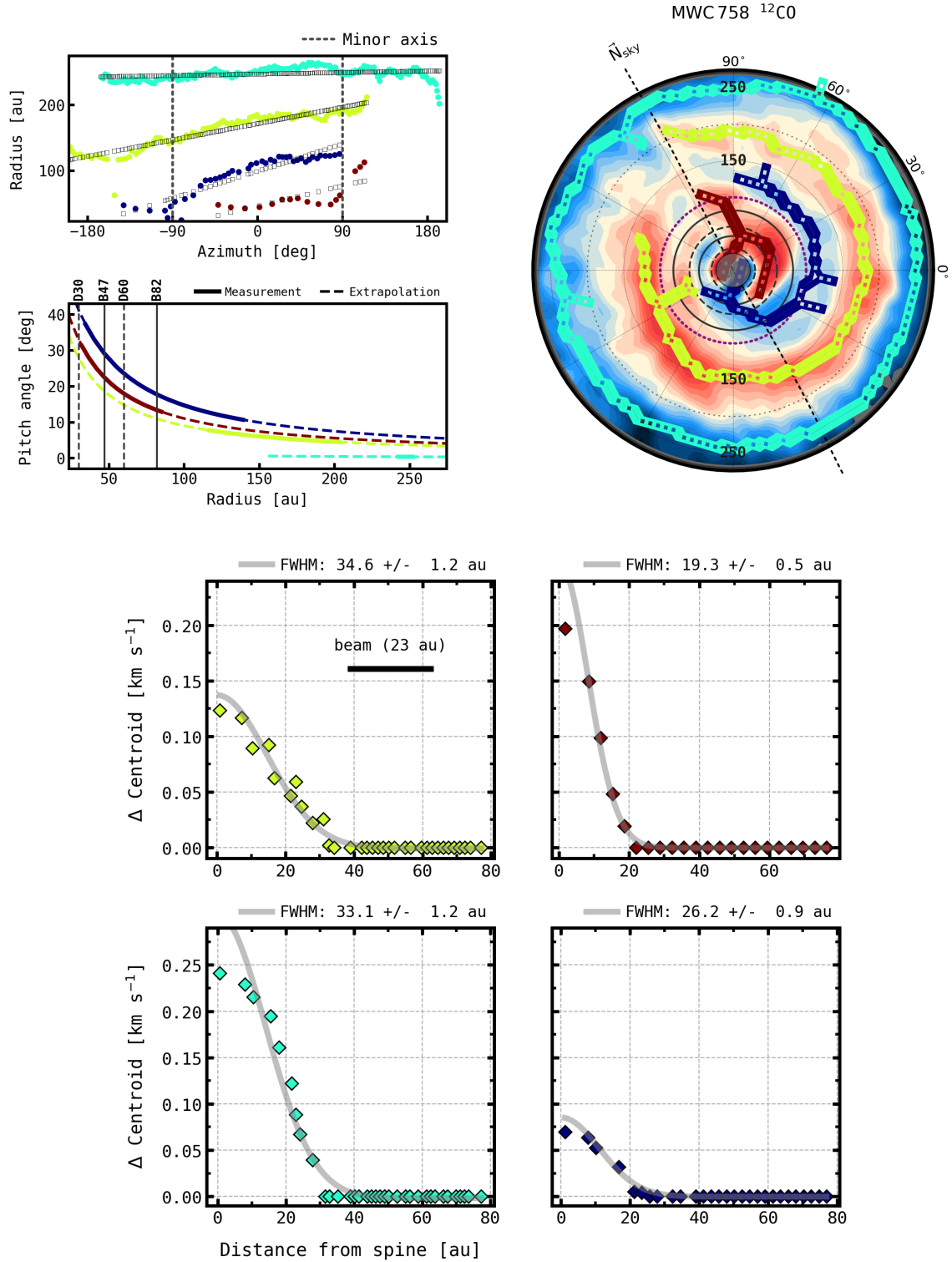


**Figure 25.** Extraction and characterization of coherent large-scale velocity substructures traced by  $^{12}\text{CO } J = 3 \rightarrow 2$  in the disc of MWC 758 using FILFINDER. The top panels illustrate the spatial configuration of the detected filaments, together with linear fits of the form  $r = a + b\phi$  used to estimate the pitch angles of the observed substructures. The main non-axisymmetric signature, traced in yellow across all panels, is well described by a tightly wound spiral with pitch angles  $< 10^\circ$  and dominated by downward vertical motions. The bottom panels display the average widths of the substructures, measured perpendicular to the medial axes of the filaments. Only the longest and outermost signatures (shown in yellow and cyan) are resolved by more than one resolution element.